Polar Low Dynamics

MICHAEL T. MONTGOMERY* AND BRIAN F. FARRELL

Department of Earth and Planetary Sciences, Harvard University, Cambridge, Massachusetts

(Manuscript received 19 July 1991, in final form 17 March 1992)

ABSTRACT

Polar lows are intense subsynoptic-scale cyclones that form over high-latitude oceans in association with deep cumulus convection and strong ambient baroclinicity. Recent observations indicate that polar lows are generally initiated by a nonaxisymmetric interaction between a surface disturbance and an upper-level mobile trough. Extant theories of polar low formation preclude study of such a process since they either constrain their models to be axisymmetric, or do not explicitly account for this transient interaction. In this work the physics of interacting upper- and lower-level potential vorticity structures is studied as an initial-value problem using a three-dimensional nonlinear geostrophic momentum model that incorporates moist processes and includes strong baroclinic dynamics. Model results illustrate the rapid formation of an intense small-scale cyclone whose structure is consistent with observations of mature polar lows.

A conceptual model of polar low development is proposed. In the first stage of development, called induced self-development, a mobile upper trough initiates a rapid low-level spinup due to the enhanced omega response in a conditionally neutral baroclinic atmosphere. A secondary development follows, called diabatic destabilization, that is associated with the production of low-level potential vorticity by diabatic processes. Diabatic destabilization represents a simple mechanism for maintaining the intensity of polar lows until they reach land. In exceptional instances of negligible upper-level forcing, the latter may also describe the gradual intensification of small-scale cyclones in regions of sustained neutrality and surface baroclinicity.

Ideas regarding polar low equilibration and prospects for a unified theory of arctic and midlatitude cyclones are discussed.

1. Introduction

Polar lows are intense subsynoptic-scale cyclones that form over high-latitude oceans, typically poleward of the polar front. Surprisingly, some of these polar cyclones bear a striking resemblance to mature tropical cyclones, including maximum surface winds of 30 m s^{-1} and a clear "eye" surrounded by deep cumulonimbi (Businger and Reed 1989a). Polar lows are distinguished from midlatitude cyclones by their relatively small scale, varying in diameter from a few hundred kilometers to more than 1000 km. Polar lows occur mainly in areas with both enhanced moist convection and large temperature contrasts associated with either the polar front or with relatively warm water adjacent to a much colder ice sheet. Smaller-scale polar lows often go undetected by synoptic observing networks as they traverse the Bering and Norwegian seas, before reaching the Alaskan and Norwegian coasts. In order to more accurately predict the formation of these storms it is important that we understand the basic dynamics of intense subsynoptic-scale cyclones in unstable air. In this work cyclogenesis and cyclone formation refer to the transformation from a weak surface disturbance into a well-developed rotary circulation, and they will be used interchangeably throughout.

Polar lows were originally thought to form from thermal instabilities within cold air masses flowing over a warm sea (Meteorological Office 1962), but a mechanism illustrating the formation of a storm-scale vortex was not proposed. Early observations alluded to the importance of mobile upper-level baroclinic disturbances in polar low formation (Harley 1960), but due to their small scale and the fact that they form mainly over the oceans, data were usually too sparse to observe the formation process or adequately resolve the interior structure. As additional data became available, polar lows were characterized as baroclinic rather than thermal instabilities (Harrold and Browning 1969). Recently, the influence of upper-level PV anomalies in promoting polar low formation has become more widely appreciated (Businger 1987; Businger and Baik 1991; Shapiro et al. 1987; Nordeng and Rasmussen 1992).

The first quantitative theory advanced to explain polar low formation was the baroclinic instability theory of Mansfield (1974). If dry-adiabatic dynamics in the absence of surface friction is used and shallow dis-

* Present affiliation: Department of Atmospheric Sciences, Colorado State University, Fort Collins, Colorado.

Corresponding author address: Dr. Michael T. Montgomery, Department of Atmospheric Sciences, Colorado State University, Fort Collins, CO 80523.

turbances with a depth of ≈ 1.6 km are assumed, this theory gives e-folding time scales of approximately 1 day for the most unstable exponential normal mode and an associated horizontal wavelength of approximately 500 km. Surface friction parameterized in the form of moderate Ekman pumping increases this e-folding time scale to 2 days and shifts the most unstable wavelength to approximately 900 km. Other inviscid baroclinic instability theories of Duncan (1977, 1978) and Reed and Duncan (1987), applied to a reversed shear flow give maximum growth rates that are slightly larger than the inviscid growth rates found in Mansfield's work. Many e-foldings are usually required in order for the most unstable normal mode to emerge from unbiased random initial conditions. However, observations indicate rapidly developing polar lows in which the full-blown mature structure emerges on time scales as short as 1 day.

The idea that polar lows are of convective origin was revived with the advent of satellite observations. Satellite images often show deep cumulus convection within polar lows, and the spiral cloud structure of some polar lows suggests that they may be related to the tropical cyclone. Rasmussen (1979) applied the theory of conditional instability of the second kind (CISK) to explain the genesis of polar lows. In the CISK theory polar lows are regarded as arising from disturbances that utilize convective available potential energy (CAPE) through a cooperative feedback between cumulus clouds and large-scale moisture convergence. The CISK theory neglects the environmental baroclinicity. A shortfall of linearized CISK theory is that the exponential growth rate is sensitive to the parameterized vertical heating distribution representing the cumulus ensemble. In certain models, for instance, if the lower atmosphere is heated more than the upper atmosphere the growth rate diverges to infinity as the disturbance wavelength tends to zero (Pederson and Rasmussen 1985; Pederson 1991). The smallest scales are favored in this case and the model does not yield a large-scale amplifying disturbance.

The inadequacy of both baroclinic instability theory and CISK for describing the formation of the variety of polar lows observed over the northern Atlantic and Pacific oceans prompted the development of mixed-instability theories that include both instability mechanisms (Sardie and Warner 1983; Craig and Cho 1988). Recent work such as the model-based diagnostic study of polar lows over the Norwegian Sea by Nordeng (1990) or the analyses of explosive cyclones in polar airstreams over the northern Pacific by Mullen (1983), however, suggest that polar lows are generally initiated and subsequently strongly influenced by mobile upper-level disturbances. The fact that these systems appear to be so strongly influenced by finite-amplitude upper-level disturbances suggests that the "selection principle," which asserts that polar lows are manifestations of the most unstable eigenmode for a particular basic-state flow, is not a useful paradigm for understanding these phenomena.

Historically, CISK was devised to describe the growth of tropical depressions into hurricanes (Charney and Eliassen 1964; Ooyama 1964), but as noted by Ooyama (1982) the acronym in common usage today no longer conveys a clear meaning. Physically speaking, the CISK closure is only valid after an incipient vortex has attained sufficient strength and organization so that the cloud-organizing mesoscales are correlated with the balanced flow (Ooyama 1982). Hence, while most analytical demonstrations of CISK are linear, the results should only physically be interpreted as describing storm intensification starting from an already well-developed circulation. An analytical CISK theory that investigates such threshold behavior has been developed by Handel (1990). In this work CISK will be regarded generically as a cooperative intensification process. Thus, although CISK may describe a portion of the intensification phase in polar lows, it does not address the formative mechanisms that produce the requisite circulations.

Recently, air–sea interaction theory has been advanced to describe the formation of the intense polar lows known as arctic hurricanes (Emanuel and Rotunno 1989). This theory emphasizes augmentation by sea surface fluxes of moist enthalpy and neglects the environmental baroclinicity. This theory also requires sufficiently well-developed axisymmetric disturbances to initiate the air–sea interaction intensification process. Starting from an axisymmetric vortex with maximum surface winds of 10 m s^{-1}, the axisymmetric model produces a hurricane strength cyclone in about 45 h; a 5 m s^{-1} initial vortex reaches hurricane strength in about 70 h. As discussed previously, observations often report shorter cyclogenesis time scales, and there is strong observational evidence suggesting that polar lows are initiated by a nonaxisymmetric interaction between upper- and lower-level finite-amplitude disturbances. While a complete description of the fully mature polar low may require taking explicit account of air–sea interaction processes, it appears from this work that the air–sea interaction intensification mechanism may not be essential for describing the basic formation process.

It is currently believed that polar low formation and growth involves a synergism among strong polar surface baroclinicity, deep moist convection, enhanced moist enthalpy fluxes, and forcing by upper-level disturbances. A number of modeling studies of polar lows have employed primitive equation models (Sardie and Warner 1985; Orlanski 1986; Gronas et al. 1987; Nordeng 1987, 1990; Emanuel and Rotunno 1989), but it is sometimes difficult to interpret the output of such models. In this work we take a complementary approach and choose a relatively simple balanced model framework to further understand polar low formation.

Previous work has confirmed the role of upper-level

interior potential vorticity disturbances in the formation of midlatitude cyclones and fronts (Eliassen and Kleinschmidt 1957; Farrell 1982, 1984, 1985; Hoskins et al. 1985; Whitaker et al. 1988; Davis and Emanuel 1990; Thorncroft and Hoskins 1990; Montgomery 1990; Montgomery and Farrell 1990, 1991, the latter is hereafter referred to as MF). Here, we investigate the influence of upper-level interior potential vorticity disturbances on polar low formation within the context of a three-dimensional geostrophic momentum model that incorporates both strong baroclinic dynamics and moist processes. In this work we are specifically interested in the physics of cyclogenesis in moist unstable air. Moist convection is modeled by assuming near-conditional neutrality, but cooperative intensification mechanisms associated with CISK or air–sea interaction are neglected.

Early theoretical work regarding baroclinically growing disturbances in unstable air focused on the effects of a reduced low-level static stability on exponentially growing eigenmodes either through explicit latent heating (Gall 1976) or with variable static stability in a dry model (Staley and Gall 1977; Blumen 1979). A decreased static stability increases eigenmode growth rates and widens the range of unstable wavenumbers to include shorter-wavelength modes. This work also suggested that exponential growth rates could be quite sensitive to reductions in the static stability, though recent work places upper bounds on their magnitude. Specifically, even in the limit of conditional neutrality growth rates have been shown to be no more than twice the growth rates of the corresponding dry system (Emanuel et al. 1987; Joly and Thorpe 1989). Rather than focusing solely on the growth rates and dynamics of individual eigenmodes modes of the linearized system, we adopt an initial-value viewpoint and shift focus to the physical objects of the theory, namely, the potential vorticity structures and their attendant thermal and momentum fields. While our model formulation is in the spirit of a reduced static stability theory, the initial-value approach produces much richer results. We show that this approach is sufficient to capture the essence of polar low formation, and a simple conceptual model of polar low development is proposed.

In section 2 we describe the mathematical model and in section 3 we present model integrations illustrating polar low formation. We conclude with a summary and discussion of our results and point to future work.

2. Model description

In this work we adopt the geostrophic momentum approximation that approximates the horizontal momentum vector by its geostrophic value. The mathematical model is based on the three-dimensional Boussinesq geostrophic momentum model (abbreviated hereafter as GM) developed by Hoskins (1975), Hoskins and Draghici (1977), and Heckley and Hoskins (1982). Moist processes are modeled as in previous work in which ascending parcels are assumed to be saturated and to conserve saturated entropy. All water rains out during the parcel's ascent and on descent the parcels conserve dry entropy (Emanuel et al. 1987; MF). It is further assumed that the combination of moist convection and sea surface fluxes maintains a state of near-moist neutrality to ascending parcels. While we acknowledge that some form of air–sea interaction is needed to maintain a state of conditional neutrality, we purposely neglect additional energy sources associated with CISK or air–sea interaction and their attendant intensification mechanisms.[1] The planetary boundary layer is parameterized with an Ekman layer (described below). Further details regarding the model formulation can be found in MF and references therein.

We believe it is justifiable to use the GM model to study polar low dynamics. The consistency of the three-dimensional GM approximation has been established for certain uniform potential vorticity flows (Hoskins 1976). More recently however, Snyder et al. (1991) have found systematic differences between the primitive equations and the geostrophic momentum equations with respect to the horizontal phase tilt of baroclinic waves and the strengths of the model anticyclones. Nevertheless, their study shows relatively small discrepancies between the strengths of the model cyclones. Thus, despite these differences in detail, the GM model appears to contain the basic elements for describing the cyclogenesis process. The mathematical and conceptual simplicity of the GM system is one of its main attractions, and it is our belief that a basic understanding of polar lows can be obtained with this system.

All tilde variables will refer to dimensional variables and nontilde variables will be dimensionless. Bold variables denote vector quantities. Nomenclature for the basic-state and disturbance-flow configurations is briefly described in terms of the modified geopotential

$$\tilde{\Phi} = \tilde{\phi} + \frac{1}{2}(\tilde{u}_g^2 + \tilde{v}_g^2).$$

The hydrostatic state for a troposphere with uniform static stability is denoted by $\tilde{\Phi}_h$. The polar tropopause is represented by an increased static stability below a rigid upper lid at $Z = H$; the tropopause part is denoted by Φ_{tr}. The static stability increases monotonically with the most rapid increase near the upper lid. The finite-

[1] It is readily demonstrated that the present moisture parameterization is CISK-less. To see this consider small quasigeostrophic disturbances about a state of rest under the influence of a linear Ekman layer at the earth's surface. In the unconditional case, a normal-mode analysis gives negative growth rates for all zonal wavenumbers provided the effective static stability is positive. We do not expect these conclusions to be essentially altered in the analogous semigeostrophic formulation with conditional heating.

amplitude flow structures that comprise the upper- and lower-level disturbances will be denoted by $\tilde{\Phi}_u'$ and $\tilde{\Phi}_l'$, respectively; their sum will be denoted by $\tilde{\Phi}'$. For simplicity we model a strong baroclinic zone by using a basic-state flow consisting of a zonally homogeneous vertical shear in thermal wind balance with a constant meridional temperature gradient; this part is denoted by $\bar{\tilde{\Phi}}$.

The model is integrated in geostrophic coordinates (X, Y, Z) given by (2.4.e–g). The choice of scaling, along with representative values, and a list of the nondimensional parameters are given in Table 1. In this work we choose a reference sea surface temperature of $\Theta_0 = 273$ K and a Coriolis parameter of $f = 1.4 \times 10^{-4}\ \mathrm{s}^{-1}$. The horizontal scale is 428 km and corresponds to the Rossby radius of deformation. The vertical scale is 6 km and represents the depth between the tropopause and the top of the boundary layer. One advective time unit corresponds to 3.96 h, the horizontal velocity scale is 30 m s^{-1}, the vertical velocity scale is 41 cm s^{-1}, and the temperature scale is 16.38 K. Scaled expressions for the total fields ($\tilde{\Phi}^{\text{total}}$, $\tilde{\Theta}^{\text{total}}$, $\tilde{\mathbf{u}}_{\mathbf{g}}^{\text{total}}$, $\tilde{w}$, $\tilde{Q}_g^{\text{total}}$) are

$$\tilde{\Phi}^{\text{total}} = N^2H^2\left[\Phi_h + \Phi_{tr} + \frac{1}{\sqrt{R_i}}(\bar{\Phi} + \Phi')\right] + gHZ$$

$$\tilde{\Theta}^{\text{total}} = \frac{\Theta_0}{g}\frac{\partial}{\partial \tilde{Z}}\tilde{\Phi}^{\text{total}} = \frac{\Theta_0 N^2 H}{g}\left[\Theta_h + \Theta_{tr} + \frac{1}{\sqrt{R_i}}(\bar{\Theta} + \Theta')\right] + \Theta_0$$

$$\tilde{u}_g^{\text{total}} = \frac{\mathbf{k}}{f} \times \tilde{\nabla}_H \tilde{\Phi}^{\text{total}} = U_0 \mathbf{u}_g$$

$$\tilde{w} = f\frac{U_0}{N}w$$

$$\tilde{Q}_g^{\text{total}} = N^2 Q_g \qquad (2.1)$$

TABLE 1. Model parameters and nondimensional flow parameters for the three-dimensional model defined in section 2. See MF for further details concerning the R parameter and see text for values used.

Model parameters:	*Dimensionless parameters:*
$N^2 = 10^{-4}\ \mathrm{s}^{-2}$	$R_i = \dfrac{N^2H^2}{U_0^2} = 4.0$
$H = 6$ km	$\delta = \dfrac{C_D U_0}{fH} = 7.14 \times 10^{-2}$
$f = 1.4 \times 10^{-4}\ \mathrm{s}^{-1}$	
$U_0 = 30$ m s^{-1}	$R = \dfrac{\Gamma_m Q_{ge}}{\Gamma_d Q_g}$
$L_R = \dfrac{NH}{f} = 428$ km	
$T = L_R U_0^{-1} = \sqrt{R_i} f^{-1} = 3.96$ h	
$C_D = 2 \times 10^{-3}$	

and

$$\Phi_h = \frac{Z^2}{2}, \quad \Theta_h = Z$$

$$\Phi_{tr} = \frac{1}{5}Z^6, \quad \Theta_{tr} = \frac{6}{5}Z^5$$

$$\bar{\Phi} = -YZ$$

$$\bar{\Theta} = -Y. \qquad (2.2)$$

The expressions for Q_g, and Φ' are given below and $R_i = N^2H^2/U_0^2$ is the Richardson number of the basic-state flow. In this work we define the potential vorticity in units of the static stability since from a dynamical viewpoint it plays the same role as the dry static stability in the transformed dimensional system. In contrast with the quasigeostrophic system, however, the equivalent dry static stability is now solution dependent and also a full function of space. For future reference, at polar latitudes one N^2 unit of potential vorticity, as defined in (2.1), corresponds to approximately 0.32 PV units as defined in Hoskins et al. (1985).

In terms of the dry potential vorticity Q_g, the nondimensional moist GM equations are

$$\left(D_g + w\frac{\partial}{\partial Z}\right)Q_g = H(w)J\frac{\partial}{\partial Z}[w^*Q_g(1 - R(Z))], \qquad (2.3.a)$$

$$D_g\Theta = 0, \quad \text{on} \quad Z = 1 \qquad (2.3.b)$$

$$D_g\Theta + \sqrt{R_i}w^*Q_g = \sqrt{R_i}H(w^*)w^*Q_g(1 - R(Z)), \quad \text{on} \quad Z = 0 \qquad (2.3.c)$$

$$Q_g\nabla_H^2\Phi' + \frac{\partial^2\Phi'}{\partial Z^2} = \sqrt{R_i}(Q_g - 1) - \frac{\partial^2}{\partial Z^2}(\sqrt{R_i}\Phi_{tr}) + \frac{Q_g}{\sqrt{R_i}}\left(\frac{\partial^2\Phi'}{\partial X^2}\frac{\partial^2\Phi'}{\partial Y^2} - \frac{\partial^2\Phi'}{\partial X\partial Y}\right),$$

$$\nabla_H^2[Q_{g_{\text{eff}}}w^*] + \frac{\partial^2}{\partial Z^2}w^* = \frac{-2}{\sqrt{R_i}}\nabla_H \cdot \mathbf{F} - \frac{1}{R_i}\frac{\partial}{\partial Z}D_g\frac{\partial(u_g, v_g)}{\partial(X, Y)}, \qquad (2.3.d,e)$$

where

A. $\nabla_H = (\partial/\partial X, \partial/\partial Y)$

B. $\partial(u_g, v_g)/\partial(X, Y) = (\partial u_g/\partial X)(\partial v_g/\partial Y) - (\partial u_g/\partial Y)(\partial v_g/\partial X)$

C. $D_g = \partial/\partial T + \mathbf{u}_g \cdot \nabla_H$

D. $\Theta = \bar{\Theta} + \Theta'$

E. $\mathbf{F} = [(\partial \mathbf{u}_g/\partial X)\cdot\nabla_H\Theta, (\partial \mathbf{u}_g/\partial Y)\cdot\nabla_H\Theta]$

F. $H(\psi)$ denotes a heaviside function such that $H = +1$ if $\psi > 0$, and $H = 0$ if $\psi \leq 0$

G. $$Q_{g_{\text{eff}}} = \begin{cases} Q_g R(Z), & \text{when} \quad w > 0 \\ Q_g, & \text{when} \quad w \leq 0 \end{cases} \qquad (2.4.a)$$

H. The moist stability parameter is given by $R(Z) = R_0 + (1 - R_0)Z^4$, and the constant R_0 is discussed below.

I.
$$w = Jw^*$$
$$J^{-1} = 1 - \frac{1}{\sqrt{R_i}}\nabla_H^2\Phi' + \frac{1}{R_i}\left(\frac{\partial^2\Phi'}{\partial X^2}\frac{\partial^2\Phi'}{\partial Y^2} - \frac{\partial^2\Phi'}{\partial X\partial Y}\right)$$
$$Q_g = J\frac{\partial}{\partial Z}\Theta^{\text{total}} \qquad (2.4.b,c,d)$$

J. The fields in physical coordinates (x, y, z) are obtained from the fields in geostrophic coordinates (X, Y, Z) via the transformation:

$$x = X - \frac{1}{\sqrt{R_i}}v_g(X, Y, Z, T)$$
$$y = Y + \frac{1}{\sqrt{R_i}}u_g(X, Y, Z, T)$$
$$z = Z. \qquad (2.4.e,f,g)$$

The GM model (2.3, 2.4) is a fully nonlinear three-dimensional model. We make no further dynamical restrictions, such as uniform interior potential vorticity. The equations (2.3) comprise two prognostic equations for the interior potential vorticity (2.3.a) and boundary potential temperature (2.3.b,c), as well as two diagnostic equations expressing invertibility (2.3.d) and thermal wind balance (2.3.e) (the latter is called the omega equation). For nonuniform interior potential vorticity we note that the omega response plays an active role in the dynamics. We also retain the nonlinear Jacobian term that is traditionally neglected in life-cycle simulations with this system. For cyclones possessing moderately large curvature vorticity, such as polar lows, asymptotic scaling arguments used to justify its neglect are no longer valid. The GM approximation,

$$\frac{D^2(u, v)}{Dt^2} << f^2(u, v),$$

formally breaks down in these circumstances, but we contend that useful physical insight can be obtained with this system even in flow regimes that exceed the limits of formal asymptotic accuracy. Further comment on this point is reserved for the conclusion.

Boundary conditions on the geopotential Φ' are that it remain doubly periodic in X and Y, and satisfy $\Theta' = \partial\Phi'/\partial Z$ along the horizontal boundaries $Z = 0, 1$. The potential vorticity is also assumed to be doubly periodic in X and Y.

We represent boundary-layer processes with a simple Ekman layer. Boundary conditions on the vertical velocity are that w (hence w^*) remain doubly periodic in X and Y; $w = 0$ on $Z = 1$; and $w = Jw^* = \delta\hat{k}\cdot\nabla_r \times \tau^{(s)}$ on $Z = 0$. In the latter, the dimensionless parameter $\delta = C_D U_0/(fH)$, ∇_r denotes the gradient operator in real coordinates (see Appendix), and $\tau^{(s)}$ is the nondimensional horizontal surface stress vector. A generalization of the quadratic stress relationship described in Gill [1982, see p. 328, Eq. (9.5.1)] that includes linear drag is given by the following:

$$\tau^{(s)} = (\beta + |\mathbf{u}_g|)\mathbf{u}_g(X, Y, 0, T). \qquad (2.4.h)$$

Using a drag coefficient of $C_D = 2 \times 10^{-3}$, the parameter values in Table 1 give $\delta = 7.14 \times 10^{-2}$. Unless otherwise stated β has been set to 0.7 in order to give an equivalent linear dimensional eddy viscosity of 24 $m^2\ s^{-1}$. Further details and properties of the lower boundary condition are discussed in the Appendix.

Since analytical solutions to the nonlinear system (2.3, 2.4) are not available a computational approach is adopted. The numerical procedure for solving (2.3) is similar to previous work (MF) except we include a second-order Arakawa finite-difference scheme for the horizontal advection term $\mathbf{u}_g\cdot\nabla_H$ (Arakawa 1966), and a second-order Shapiro filter on the potential vorticity field at each time step to suppress computational noise (Robinson and Walstad 1987). The elliptic equations (2.3.d,e) are solved with SOR. The potential vorticity and boundary potential temperature are minimally corrected within each time step to ensure solvability of (2.3.d). The Jacobian term in the omega equation is evaluated after Φ' is determined from (2.3.d), and its local time derivative is approximated with an Euler difference.

The computational domain consists of a rectangular cube whose X, Y, and Z dimensions are L_X, L_Y, and 1, respectively. In this work we have chosen $L_X = L_Y = 5$, corresponding to a horizontal domain of 2190 km × 2190 km. A sketch of the computational domain is given in Fig. 1. Let L, M, and N denote the number of panels in the X, Y, and Z directions, respectively. The horizontal grid increments in geostrophic space are then $\delta X = L_X/L$, and $\delta Y = L_Y/M$, whereas the vertical grid increment is $\delta Z = 1/N$. With $L = M = 32$

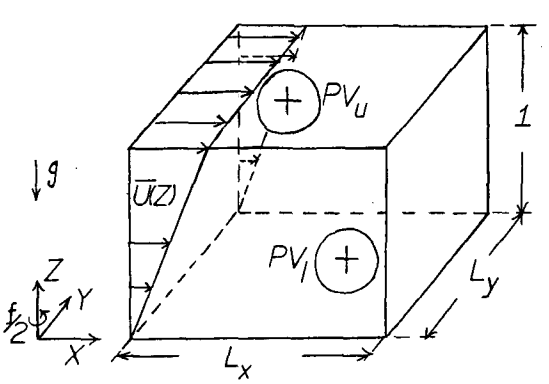

FIG. 1. Three-dimensional model geometry for the basic-state flow defined in section 2, and a sketch of the initial flow given by (3.1.a) in section 3. PV_u and PV_l denote the upper- and lower-level potential vorticity anomalies, respectively.

and $N = 16$, this corresponds to a horizontal grid resolution in geostrophic coordinates of 66.8 km, and a vertical grid resolution of 375 m. The nondimensional time-step increment used in this work is $\delta T = 1/36$, and corresponds dimensionally to 6.6 minutes. Results of the upcoming section were determined to be adequately converged at this resolution.

The transformation from geostrophic coordinates to real coordinates compresses regions where J is greater than unity and stretches regions where J is less than unity. Consequently, regions of strong cyclogenesis are well resolved and the coordinate transformation often more than doubles the resolution in these regions.

Finally, for completeness we briefly summarize the moisture parameterization. In a conditionally stable atmosphere the equivalent moist potential vorticity is positive. The moist stability parameter, R, satisfies $0 < R < 1$, and thermodynamic considerations place lower bounds on the magnitude of R. At very low temperatures R approaches unity, the PV induction term on the rhs of (2.3.a) is small, and the effective static stability in the omega equation, (2.4.a), is of order unity (MF). Hence, moist processes only slightly alter dry-adiabatic dynamics in very cold stable air.

On the other hand, in a conditionally unstable saturated atmosphere the moist equivalent potential vorticity is negative, that is, R is negative in moist unstable air. Hence, while thermodynamic constraints are still operative, R is more strongly controlled by vertical instability and the internal dynamics of moist convection. In this case the PV induction term is potentially of order unity, and the effective static stability is negative in ascending regions. This suggests that even in relatively cold environments, condensational processes are an important component of cyclone dynamics in moist unstable air.[2] As a first approximation we retain our original assumption: moist unstable regions associated with unlimited moisture supply are modeled by taking R small and positive.

The specific moist stability parameterization given by H above corresponds physically, as $R_0 \to 0$, to a moderately deep moist neutral region with a rapid adjustment to a strongly stable region near the tropopause. Horizontal variations in R are considered secondary compared to vertical variations. To model a nearly moist neutral atmosphere in the Arctic we have chosen $R_0 = 0.1$ for the majority of examples discussed in the next section.

3. Computational results

Solutions of the three-dimensional model (2.3, 2.4) have been checked for several cases. For dry inviscid dynamics ($R = 1.0$), the model has verified the growth rate, phase speed, and the nonlinear structure of the most unstable square Eady wave possessing uniform potential vorticity as discussed in Hoskins (1976). For moist inviscid dynamics, this model duplicates results of previous work for strictly two-dimensional disturbances (MF). For cyclogenesis time scales on the order of one day, condensational processes also did not introduce growing three-dimensional disturbances into simulations initialized with strictly two-dimensional disturbances. In the general three-dimensional case, the numerical model exhibits convergence as the spatial and temporal increments go to zero.

A flow configuration observed to precede polar low formation consists of an upper-level trough positioned upstream of a surface disturbance (Shapiro et al. 1987; Nordeng 1990; Nordeng and Rasmussen 1992; Businger 1991). Physically, the upper disturbance is a mobile upper-tropospheric trough. The surface disturbance could originate from any of the following: an outbreak of cold air flowing southward over the ice sheets; remnants of a surface front; an occluded cyclone that formed farther upstream; or vorticity debris to the rear of a cold front as suggested recently by Schär and Wernli (1991) in an initial-value simulation of midlatitude dry cyclogenesis. Previous work has demonstrated favorable conditions for rapid surface development involving upper-level interior potential vorticity disturbances in linear quasigeostrophic (Farrell 1982, 1984) and two-dimensional semigeostrophic nonlinear balanced models (Montgomery 1990; Montgomery and Farrell 1990, 1991). Here, we study the nonlinear physics of the three-dimensional moist interaction between these dynamical entities.

The initial configuration is modeled by an upper-level potential vorticity anomaly upstream of a lower-level potential vorticity anomaly. A sketch of the initial flow is given in Fig. 1. East is defined as positive X and north is defined as positive Y. Of course, the solution phase space spanned by (2.3, 2.4) is large and an exhaustive study of various flow configurations has not been attempted. As far as the basic physics is concerned, however, we believe the examples given below are representative realizations of atmospheric flow processes. Letting u and l denote the upper and lower disturbances, respectively, expressions for these disturbances in geostrophic space are:

$$\Phi'_u = \frac{A_u}{1 + 1.5\,R_u^2}\,\frac{1}{1 + 4.0(Z - Z_u)^2}$$

$$\Phi'_l = \frac{A_l}{1 + 0.5\,R_l^2}\,\frac{1}{1 + 6.0(Z - Z_l)^2} \qquad (3.1.a)$$

where

$$R_u^2 = (X - X_u)^2 + (Y - Y_u)^2$$

$$R_l^2 = (X - X_l)^2 + (Y - Y_l)^2$$

$$A_u = -\frac{12}{40}, \quad A_l = -\frac{15}{40}. \qquad (3.1.b)$$

[2] This viewpoint complements previous work (MF) since here we investigate cyclone formation in moist unstable air.

The upper disturbance is centered at $(X_u, Y_u, Z_u) = (2.1, 2.25, 0.6)$, and the lower disturbance is centered at $(X_l, Y_l, Z_l) = (3.1, 2.25, 0.1)$. We note that initial discontinuities in spatial derivatives of (3.1) on lateral boundaries are quickly damped and do not disrupt the cyclogenesis processes described below.

The relative vorticity of the upper disturbance is approximately $1.5f$, while the lower disturbance has a relative vorticity maximum on $Z = 0$ of approximately $0.2f$. The horizontal scale of the upper-level anomaly is approximately 450 km, and is commensurate with observations of upper-level troughs in the polar atmosphere.

First consider dry dynamics. From previous work (MF) the local nondimensional Rossby penetration depth, R_{pen}, for both elliptic equations (2.3.d,e) varies as $1/k\sqrt{Q_g}$, where k is the characteristic wavenumber of the PV anomaly under question. The expression for R_{pen} is strictly valid only for slowly varying PV anomalies, but we expect a qualitatively similar result for localized anomalies. In (3.1) for example, this suggests that R_{pen} is less than 1/6. Small-scale PV anomalies will thus have smaller penetration depths than large-scale anomalies. Baroclinic coupling between anomalies PV_1 and PV_2 is typically measured by the meridional heat flux correlation between these structures defined by $\overline{v_{g1,2}\theta_{2,1}}$, where the overbar denotes a horizontal integral. It follows that baroclinic coupling will be weaker for small-scale upper anomalies than for large-scale upper anomalies. Thus for small-scale PV anomalies confined near the tropopause and the surface, only minimal surface development is expected.

Moist neutral dynamics can be drastically different. Although the penetration depth for (2.3.d) is formally unchanged by moist processes, the penetration depth of the omega equation is substantially increased in moist neutral regions. In these cases there is increased omega coupling between upper- and lower-level disturbances and hence far greater cyclogenesis potential. We find rapid cyclogenesis in this case, and results are shown in Figs. 2a–f. Salient features are discussed below.

a. Potential vorticity and vertical velocity

Figure 2a shows three snapshots of the total potential vorticity field Q_g at $T = 0$, 2, and 6.4 advective times corresponding to 0, 7.92, and 25.3 h, respectively. Contour plots of horizontal sections of Q_g are shown in the left column of Fig. 2a, while the right column shows vertical cross sections. Vertical cross sections correspond to y = constant planes taken through the absolute vorticity maximum on $Z = 0$. Figure 2b shows the vertical velocity in the same format as Fig. 2a, but note the changing contour interval.

Initially, the upper potential vorticity anomaly is slightly underneath the tropopause layer and has an initial horizontal scale of approximately 500 km. The upper-level anomaly induces ascending motion in front of it and descending motion behind it. The maximum vertical velocity occurs at approximately $Z = 0.45$. There is a secondary vertical velocity maximum in front of the lower potential vorticity anomaly. We recall from previous work (MF) that the assumption of conditional moist neutrality produces an asymmetry in the vertical motion response. At $T = 0.0$ the upward velocity is approximately twice as strong as the downward velocity, and the region of rising air is narrower and deeper than the region of descending air.

By $T = 2$, the upper anomaly has moved toward the lower anomaly and surface potential vorticity is generated in a local region near $(x, y) = (3.7, 2.5)$ within the initial low-level disturbance. Also at this time maximum ascent is found at $Z = 0.3$ with an upward velocity of 0.16 (6.7 cm s^{-1}). At the top of the boundary layer ($Z = 0.0$) the upward velocity has a maximum of 0.11 (4.5 cm s^{-1}), and coincides with the induced potential vorticity maximum. By $T = 6.4$ the vortex couplet has traveled out the right side of the computational domain and entered the western side (x periodicity). The surface potential vorticity has greatly increased between $T = 2.0$ and $T = 6.4$ and an intense small-scale cyclone emerges near $(x, y) = (0.8, 3.28)$. The maximum dimensionless potential vorticity on $Z = 0.0$ increases from 3.49 at $T = 0.0$ to 13.36 at $T = 6.4$, corresponding to a dimensional increase from 1.11 to 4.27 PV units. At $T = 6.4$ the vertical velocity maximum is now found on $Z = 0.0$ and has a magnitude of 1.76 (73.9 cm s^{-1}). At this time we also note that the y section of the vertical velocity resembles the primitive equation simulations of Nordeng (1990; see his Figs. 10b and 12).

The surface potential vorticity maximum at $T = 6.4$ is almost surrounded by air rising out of the boundary layer. At upper levels, the field of ascending motion acquires a more north–south orientation, but still tends to surround the surface potential vorticity maximum (not shown). It is also worth noting that the region of maximum ascent at upper levels is slightly eastward of the surface potential vorticity maximum. The structure of the ascending flow resembles the observations of Harrold and Browning (1969; see their Fig. 7) and is consistent with satellite images showing cloud patterns partially encircling polar lows (Reed 1979; Rasmussen 1985; Shapiro et al. 1987).

Disturbances at middle levels can be influenced by the newly formed cyclone. In this example the middle portion of the upper potential vorticity anomaly travels around the southern side of the surface anomaly instead of directly over it. The uppermost portion of the anomaly is deflected only slightly southward as it passes over the induced cyclone (not shown).

As previously discussed (MF), latent heat release in ascending regions generates potential vorticity at low levels and depletes potential vorticity at upper levels. For inviscid flow in the absence of explicit sea surface

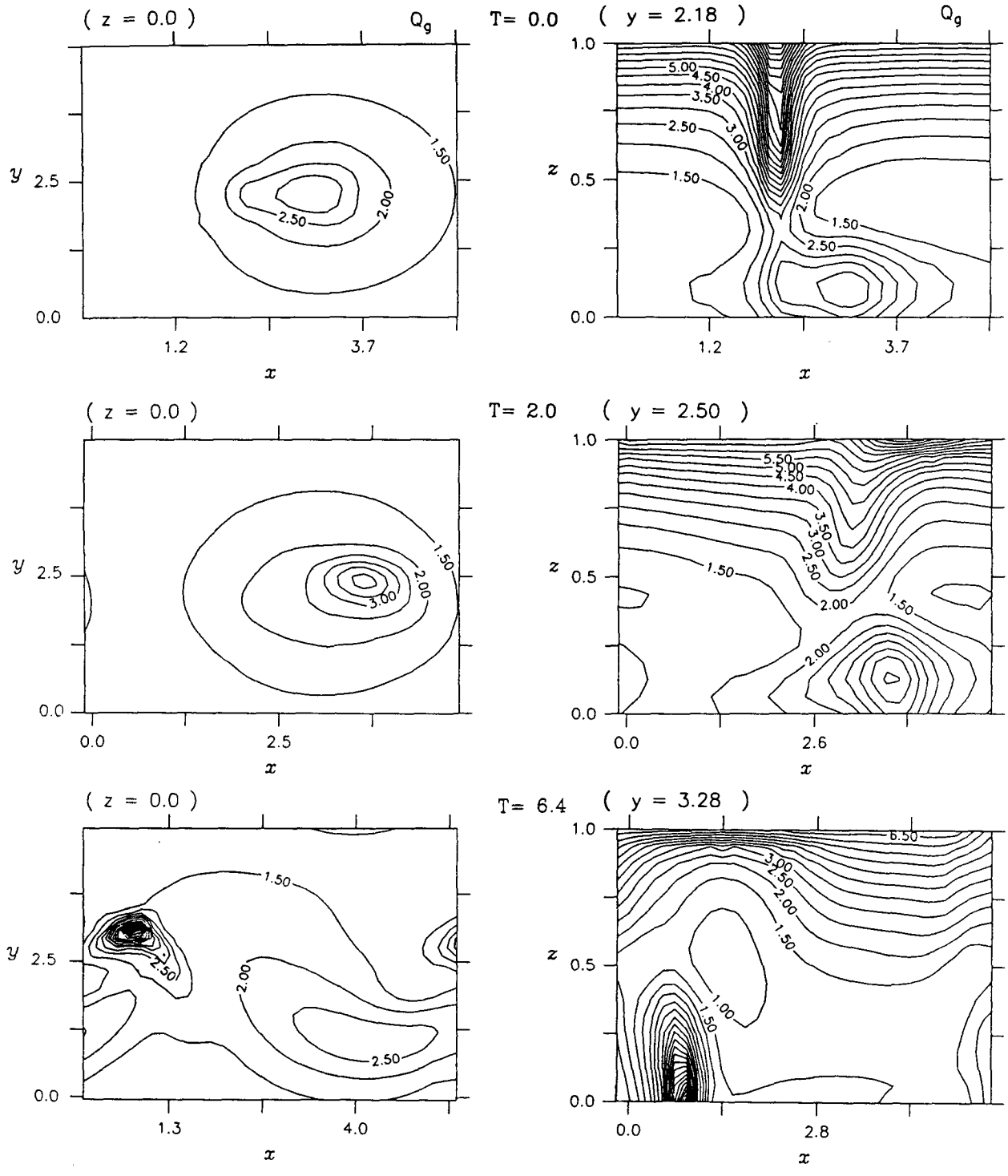

FIG. 2a. Snapshots of moist dynamics ($R_0 = 0.1$) for the three-dimensional initial condition given by (3.1.a) at $T = 0$, 2, and 6.4 advection times (0.0 h, 7.96 h, and 25.3 h, respectively). Shown are contour plots of the nondimensional total potential vorticity Q_g at the top of the boundary layer $Z = 0.0$, and through a y section corresponding to the maximum absolute vorticity on $Z = 0.0$. The contour interval is fixed at 0.50. Solid lines denote positive values. The dimensional potential vorticity is obtained via $\tilde{Q}_g = N^2 Q_g$. (One N^2 unit corresponds to approximately 0.32 PV units.)

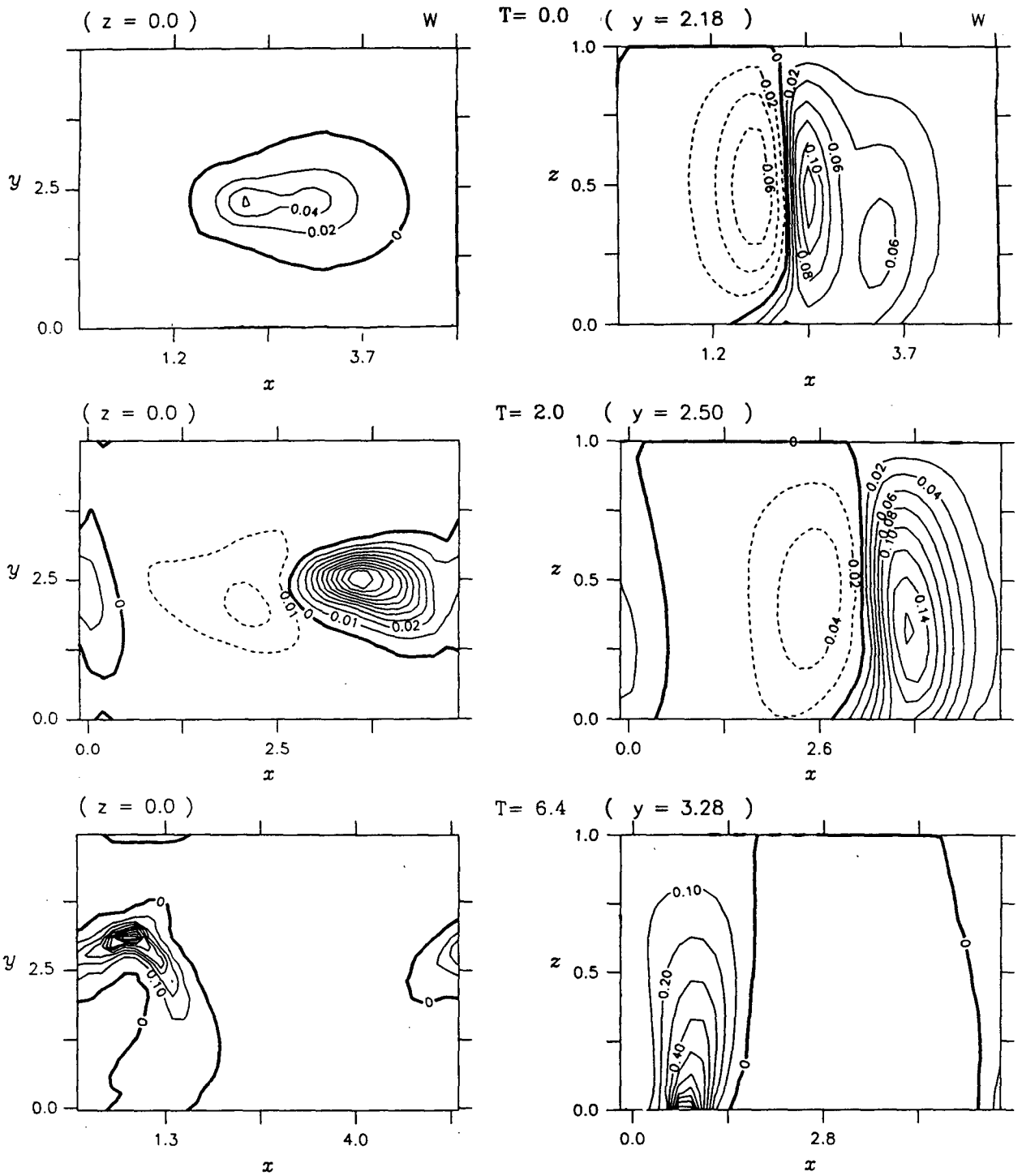

FIG. 2b. As in (a). Shown are contour plots of the nondimensional vertical velocity w at the top of the boundary layer $Z = 0.0$, and through a y section corresponding to the maximum absolute vorticity on $Z = 0.0$. Note that the contour interval changes with time and is generally different for each plot. A unit value of w corresponds to 41 cm s^{-1}. Solid lines denote positive values and dashed lines denote negative values.

fluxes, the mass-weighted integral of potential vorticity does not change (Hoskins et al. 1985). We find that Ekman pumping only slightly alters this result (see Appendix). However, the interaction between upper- and lower-level potential vorticity disturbances can be strongly influenced by the creation of local sources and

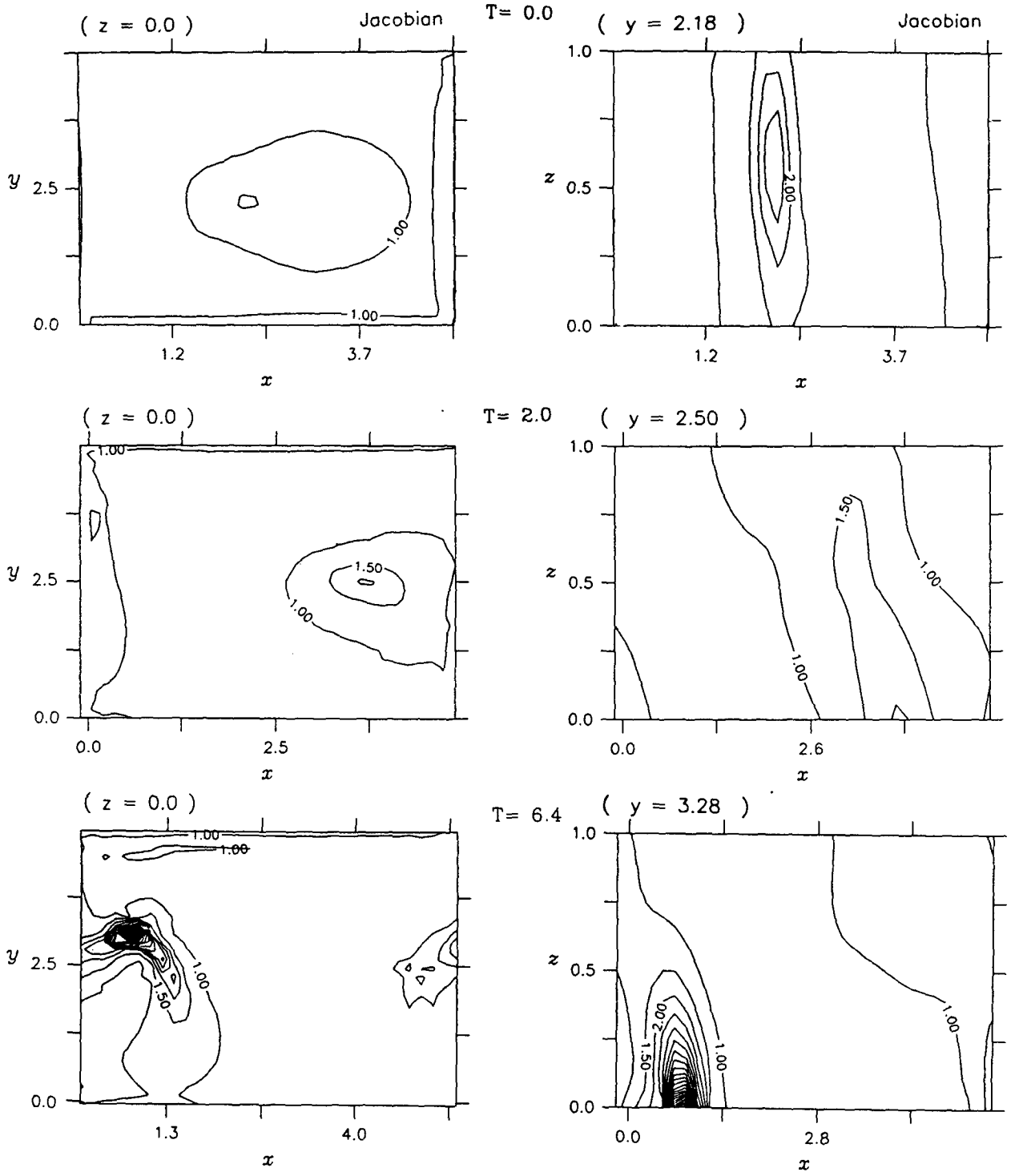

FIG. 2c. As in (a). Shown are contour plots of the Jacobian ($= \omega_{abs} \cdot \hat{\mathbf{k}}/f$) at the top of the boundary layer $Z = 0.0$, and through a y section corresponding to the maximum absolute vorticity on $Z = 0.0$. The contour interval is fixed at 0.50. Solid lines denote positive values.

sinks of potential vorticity. The potential vorticity structure for this example is mainly tripolar in structure. The three contributions are: the intense surface potential vorticity maximum (cyclone); a midlevel potential vorticity minimum downstream of the cyclone; and a midlevel potential vorticity maximum south of the cyclone that originated from the initial disturbance aloft.

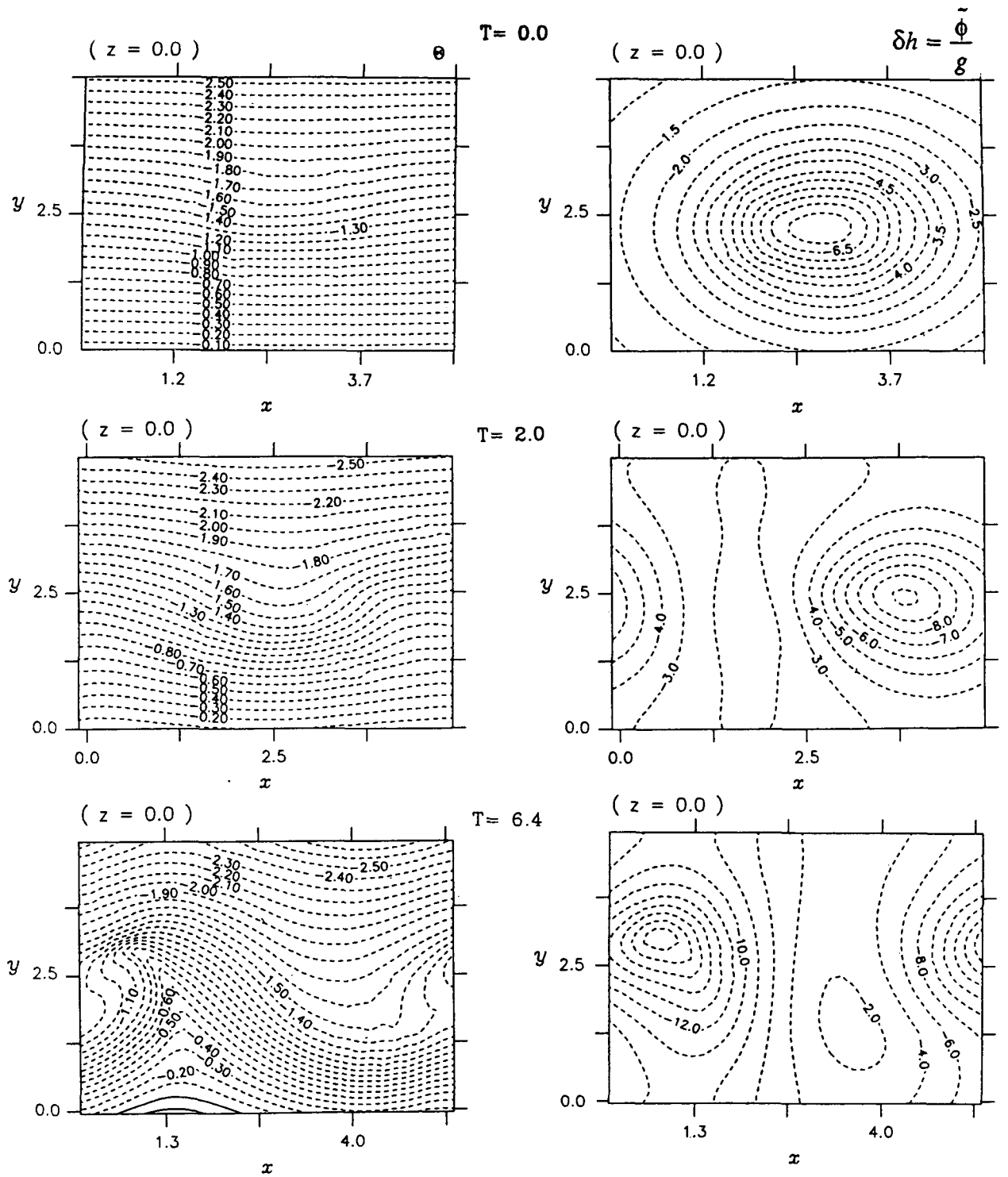

FIG. 2d. As in (a). In the left column are contour plots of the potential temperature θ at the top of the boundary layer $Z = 0.0$. The height field $\delta h \equiv \tilde{\phi}/g$ on $Z = 0.0$ in decameters (dm) is shown in the right column. The contour interval for θ does not change, but the contour interval for δh changes for each plot. A unit value of θ corresponds to 16.3 K, and a unit value of δh corresponds to approximately 1.2 mb. Dashed lines denote negative values.

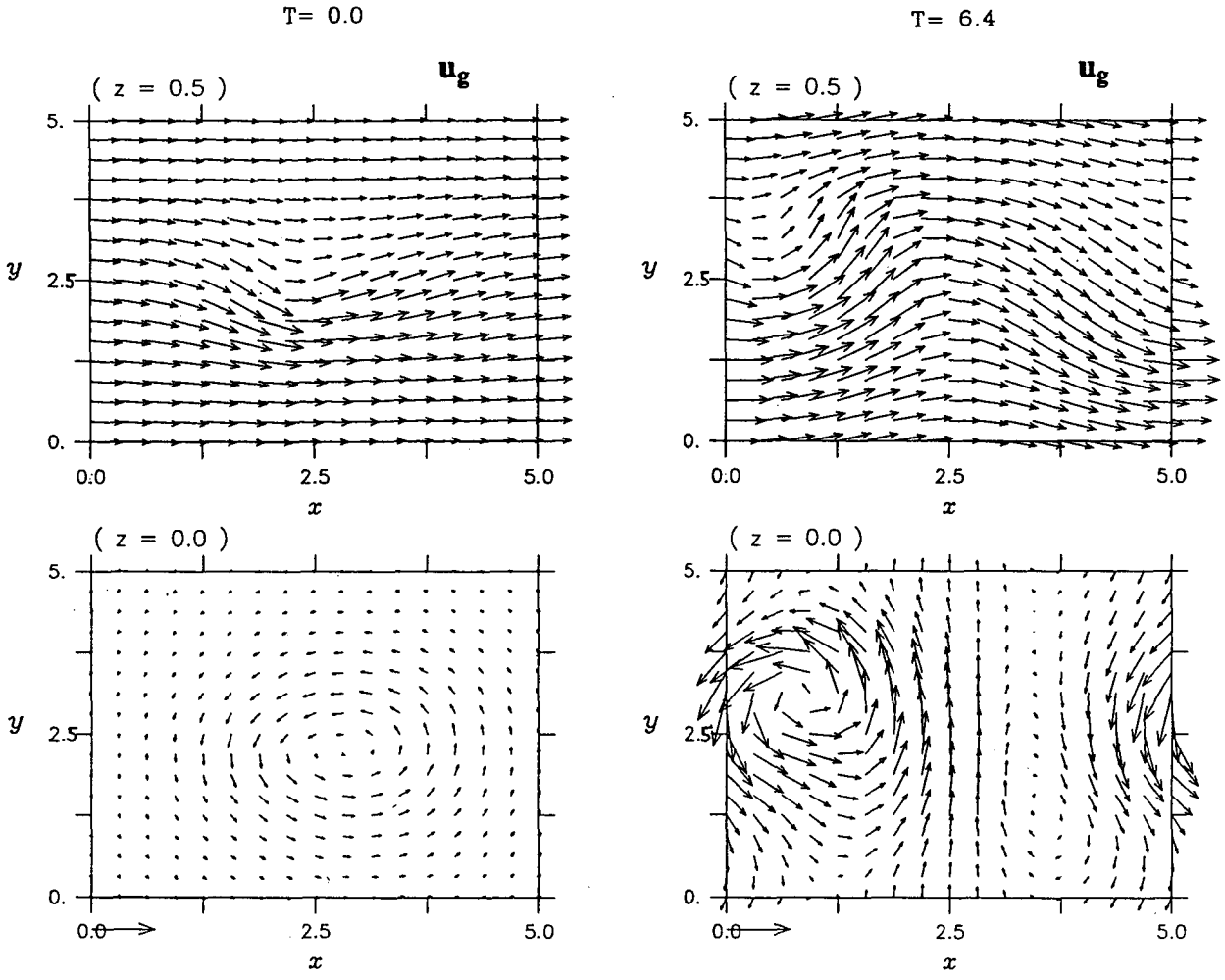

FIG. 2e. Snapshots of moist dynamics ($R_0 = 0.1$) for the three-dimensional initial condition given by (3.1.a) at $T = 0$ and 6.4 advection times (0.0 h and 25.3 h, respectively). Vector plots of the nondimensional geostrophic winds $\mathbf{u}_g$ in geostrophic coordinates are shown in each column. The winds at $Z = 0.5$ ($\approx$500 mb) are displayed in the upper plot, and the winds on $Z = 0.0$ are displayed in the lower plot. The horizontal vector in the bottom left corner of each vertical pair corresponds to 30 m s^{-1}. Note that the scale contraction implied by (2.4.e,f) is not included in this plot.

b. Absolute vorticity

Figure 2c shows the nondimensional Jacobian [J in (2.3, 2.4)] at $T = 0.0$, 2.0, and 6.4 advection times (0.0, 7.96, and 25.3 h, respectively) in the same format as Fig. 2a. Since the Jacobian and the nondimensional vertical component of absolute vorticity are equal, they will be referred to interchangeably.

At $T = 0.0$ the vertical structure of the absolute vorticity field tilts slightly westward with height, and indicates a favorable configuration for extracting available potential energy from the basic state. A rapid spinup of absolute surface vorticity occurs at later times. At $T = 2.0$ the maximum absolute vorticity occurs at the surface with a maximum of $2.0f$. At $T = 6.4$, the absolute vorticity on $Z = 0.0$ has increased to $20.0f$. Magnitudes are consistent with observations taken from a research flight through a polar low that report relative vorticities of approximately $20f$ near the storm's center (Shapiro et al. 1987).

The scale contraction evident in the vorticity field and other fields discussed below is a very striking feature of these examples. This effect is implicit in the nonlinear transformation from geostrophic coordinates back to real coordinates via Eq. (2.4.e,f). Consider the Jacobian field on $Z = 0.0$ at $T = 6.4$. The region with Jacobian greater than 1.5 is crescent shaped; its southern portion is associated with the cold front; and its central portion is associated with the surface potential vorticity maximum. The width of this region is much smaller than one horizontal unit, a Rossby radius (428 km). Thus, if either the surface absolute vorticity or potential vorticity were used as proxy for indicating a cyclone's scale, then this model cyclone would surely be classified as subsynoptic. The cyclone's radius of maximum winds and frontal scale (discussed shortly)

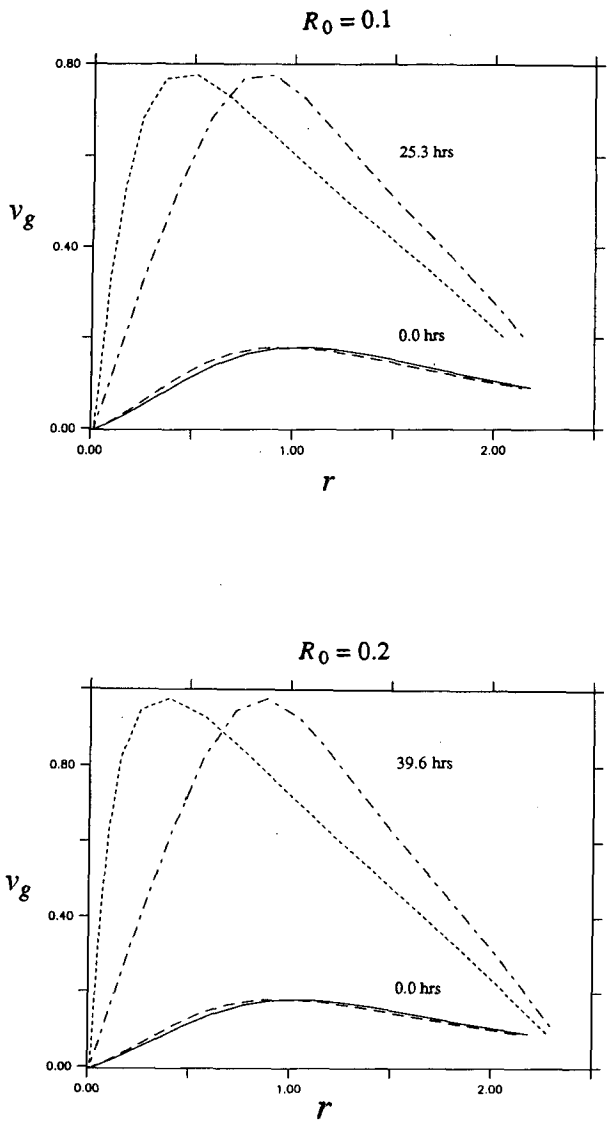

FIG. 2f. Meridional geostrophic wind v_g on $Z = 0.0$ versus eastward distance r from the storm center. The top and bottom plots correspond to the simulation with $R_0 = 0.1$ and $R_0 = 0.2$, respectively, and the Y section corresponds to the maximum absolute vorticity. Shown are the initial and final radial wind distributions in both geostrophic and real coordinates. A unit value of v_g corresponds to 30 m s^{-1}, and a unit value of r corresponds to 428 km. The innermost curve for each pair is the wind distribution in real coordinates. The radius of maximum wind for v_g in real coordinates is 219 km and 168 km for $R_0 = 0.1$ and $R_0 = 0.2$, respectively. These plots are not symmetric averages.

tend to corroborate this classification. Numerical integration was terminated at $T = 6.4$ since the Jacobian rapidly increased shortly thereafter. Remarks concerning the tendency of this model to "blow up" in finite time and a discussion of this cyclone's ultimate horizontal scale are reserved for the conclusion.

c. *Thermal structure*

The left column of Fig. 2d shows three contour plots of the potential temperature field Θ on $Z = 0$ for the same times as Fig. 2a. The environmental meridional temperature gradient is approximately 18 K/1000 km. The cold thermal perturbation associated with the potential vorticity disturbances aloft is found in the center of the model domain. As time increases the thermal contours become wrapped around the induced cyclone. By $T = 6.4$ a cold front has formed to the southwest of the cyclone and is advancing toward the southeast. There is also a warm front on the cyclone's northwest flank. The frontal configuration resembles the bent-back warm front and frontal T-bone of Shapiro et al. (1990). Observations in the vicinity of polar lows show similar frontal structures (Mullen 1983; Shapiro et al. 1987).

At $T = 6.4$ a tongue of warm air intrudes into colder air, and its end portion resides in the storm's southwestern sector. Cold air has been drawn southward and begins to encircle the warm tongue. Flight observations within a polar low report a warm region near the storm's center but on its southwest side (see Fig. 12 of Shapiro et al. 1987). The process by which warm air becomes cut off from its parent source and gets surrounded by colder air is termed "warm air seclusion."

d. *Height field*

The right column of Fig. 2d displays the height field $\delta h \equiv \tilde{\phi}/g$ for $Z = 0$. At $T = 0$ the height perturbation anomaly over the model domain has a deficit of 6.5 dam (7.8 mb pressure deficit). The vortex couplet produces the elliptical height contours at $T = 0.0$. At early times the upper-level height anomaly overtakes the low-level anomaly, but at later times the upper- and low-level height anomalies become almost vertically aligned. The surface height field drops rapidly as the couplet travels out the right side of the domain and enters the western side. The height field anomaly at $T = 6.4$ is 22.3 dam (26.7 mb pressure deficit). The pressure drops approximately 19 mb in a 25-h period. A barograph plot (not shown) gives no indication of pressure filling at $T = 6.4$, and other numerical experiments indicate that it would continue deepening at later times. Also note the reduction in scale of the surface height field anomaly.

e. *Horizontal winds*

Vector plots of the nondimensional geostrophic winds $\mathbf{u}_g$ in geostrophic coordinates are shown in Fig. 2e. Displayed are horizontal cross sections of the geostrophic winds at midlevel ($Z = 0.5$) and the top of the boundary layer ($Z = 0.0$). The horizontal vector in the bottom left corner of each vertical pair of plots corresponds to 30 m s^{-1}. The scale contraction near the cyclone implied by the transformation (2.4.e,f) is not included in this plot. In real coordinates the radius of maximum winds would be even closer to the storm center. The effect of the transformation from geostrophic coordinates back to real coordinates is illustrated in Fig. 2f.

At $T = 0.0$, the upper-level potential vorticity anomaly produces cyclonic flow in the upper westerlies. On $Z = 0.0$ the initial winds indicate a weak large-scale cyclonic gyre. As the upper disturbance approaches the surface disturbance the surface winds rapidly intensify. The maximum geostrophic winds on $Z = 0.0$ increase from 0.21 at $T = 0.0$ to 0.90 at $T = 6.4$. Dimensionally, this corresponds to an increase from 6.5 m s^{-1} to 27 m s^{-1} in 25 h. The maximum in the total horizontal winds $\mathbf{u}_T = \mathbf{u}_g + \mathbf{u}_a$ (not shown) increases from 5.4 m s^{-1} to approximately 40 m s^{-1} in the same 25-h period. The supergeostrophic winds are confined to the cyclone's northeastern sector, and the total winds do not appear to be circularly symmetric about the center of minimum pressure. We note that supergeostrophic winds are not prohibited in rapidly developing extratropical cyclones.

If, for the same flow configuration, the moist stability parameter is increased to $R_0 = 0.2$ rapid cyclogenesis is also found though at a slightly reduced rate. In this case (not shown) a mature polar cyclone emerges at $T = 9.0$ (35.6 h) with an absolute vorticity maximum of $20f$, maximum geostrophic surface winds of 33 m s^{-1}, a surface height anomaly of 28.3 dam ($\approx$34 mb pressure deficit), and a similar frontal structure. Figure 2f shows the radial distribution of the meridional geostrophic wind for both the $R_0 = 0.1$ and $R_0 = 0.2$ experiments. The rapid increase in wind speed and the scale contraction of the radius of maximum winds are noteworthy features of both plots. The $R_0 = 0.2$ case has an even smaller radius of maximum wind ($\approx$170 km) since the storm was able to develop further before singularity formation. Further comment regarding the ultimate cyclone scale is reserved for the conclusion.

To assess the importance of condensational processes in the preceding examples, results for dry-adiabatic dynamics ($R \equiv 1.0$) are displayed in Fig. 3. The first plot is a y = constant cross section of Q_g at $T = 4.0$ (15.8 h). The second and third plots correspond, respectively, to the potential temperature and geostrophic winds on $Z = 0.0$ at $T = 10.0$ (39.6 h).

In the dry case there is no surface potential vorticity generation on $Z = 0.0$ and the upper potential vorticity anomaly passes over the surface potential vorticity with minimal baroclinic interaction. The maximum absolute vorticity resides at upper levels early in the integration. A weak spinup of vorticity on $Z = 0.0$ does occur at later times, with a maximum absolute vorticity of $1.87f$ at $T = 10.0$ (not shown). The temperature contours at $T = 10.0$ show warm air intruding into colder air, but the frontal structure is weaker than both runs previously discussed. Warm-air seclusion has not occurred by $T = 10.0$. On $Z = 0.0$ the maximum geostrophic winds are 9 m s^{-1}, 12 m s^{-1}, and 18 m s^{-1} at $T = 4.0$, 6.0 and $T = 10.0$, respectively.

Evidently, for upper-level PV anomalies with horizontal scales near the ambient deformation radius, the condensation process is essential for the storm's rapid spinup, small horizontal scale, and large absolute vorticities. Physically, in order to maintain thermal wind balance in the presence of a small static stability in ascent regions, stronger ascending currents are required. This strong ascent results in vortex stretching at low levels and generation of surface potential vorticity that then augments the baroclinic interaction between these systems.

We also note that while there are slowly growing unstable modes present in these calculations (with *e*-

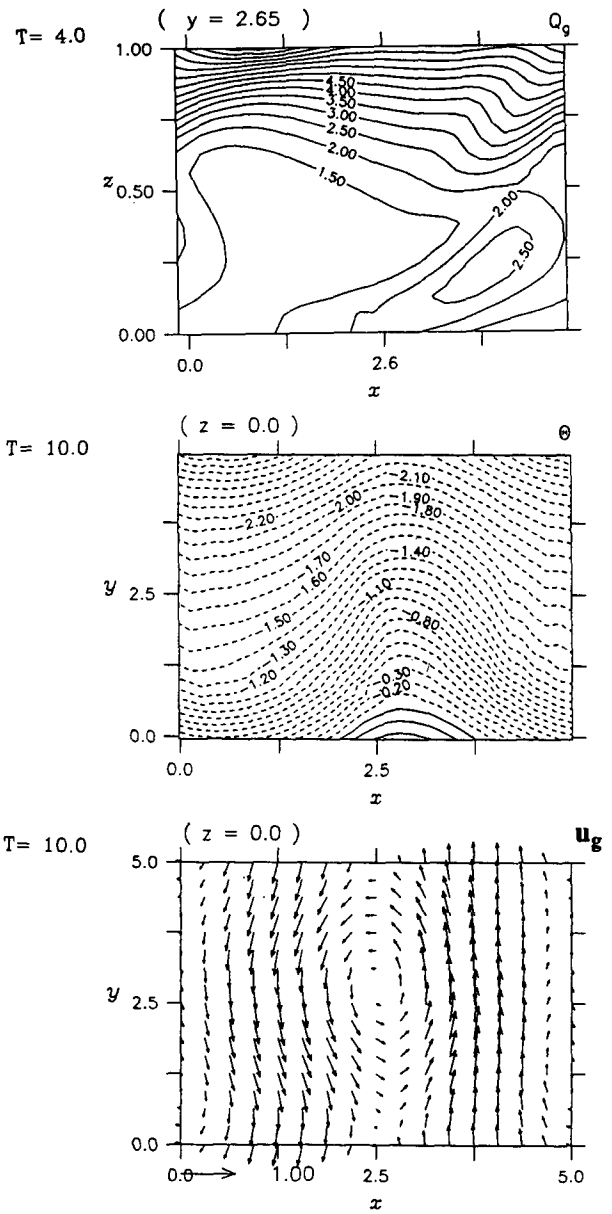

FIG. 3. Dry-adiabatic dynamics ($R \equiv 1.0$) for the same three-dimensional initial condition given by (3.1a) at $T = 4.0$ and $T = 10.0$ advection times (15.8 h and 39.6 h, respectively). At the top a y section of Q_g at $T = 15.8$ h along $y = 2.65$ is shown. The contour interval is 0.5. The middle plot displays the potential temperature θ on $Z = 0.0$ at $T = 39.6$ h. The geostrophic winds on $Z = 0.0$ are shown in the bottom plot. Contour and plotting conventions are the same as in Figs. 2d and 2e.

folding times greater than cyclogenesis time scales), they have insufficient time to have a significant impact on the cyclogenesis process. In these examples, the simulated cyclones rapidly become nonlinear entities. These occluded structures result from a nonlinear evolutionary process and are not usefully viewed as the asymptotic emergence of the most unstable eigenmode of a linear eigenvalue calculation.

Previous work investigated a secondary development phase, called diabatic destabilization, associated with the generation of potential vorticity in ascent regions at low levels (MF). This secondary development has no counterpart in dry-adiabatic dynamics. In the first two examples this process follows the PV interaction. To focus on this process the model is initialized with just a low-level potential vorticity disturbance of similar form as (3.1), but with maxima on $Z = 0.0$. The disturbance is given by

$$\Phi'_u = 0.0$$

$$\Phi'_l = \frac{A_l}{1 + 1.0R_l^2} \frac{1}{1 + 6.0Z^2} \tag{3.2}$$

where

$$A_l = -\frac{10}{40},$$

R_l is the same as in (3.1), and the lower disturbance is centered at $(X_l, Y_l, Z_l) = (2.5, 2.5, 0.0)$. A value of $R_0 = 0.1$ is used for the moist stability parameter and the Ekman pumping strength is as in Table 1.

Figure 4a shows a y = const cross section of Q_g and the Jacobian fields at $T = 0.0$ and $T = 10.0$. Figure 4b shows horizontal sections of Q_g and the geostrophic winds on $Z = 0.0$ at the latter time. By $T = 10.0$, a moderate spinup along $Z = 0.0$ has occurred in association with the generation of low-level potential vorticity in ascent regions. Also note that by this time the surface vortex has traveled out the right side of the model domain and entered the west side of the domain. The induced low-level potential vorticity is strongly localized and has an attendant cyclonic circulation around it. The maximum absolute vorticity on $Z = 0.0$ increases from $1.75f$ at $T = 0.0$ to $6.53f$ at $T = 10.0$, while the nondimensional surface potential vorticity increases from 4.31 to 7.69. The latter corresponds to an increase from 1.37 to 2.46 PV units. The potential vorticity structure at $T = 10.0$ is dipolar with a potential vorticity maximum near the surface and a midlevel potential vorticity minimum downstream of the surface maximum. As discussed in previous work (MF) this configuration results in a poleward heat transport converting available potential energy into disturbance energy. The maximum geostrophic surface winds increase from 4.5 to 20.7 m s^{-1} by $T = 10.0$. As in the previous examples, the resultant vortex is a localized nonlinear structure. It is the product of an evolutionary process, and not simply the asymptotic emergence of the most unstable eigenmode of a linear eigenvalue calculation.

Previous work investigated diabatic destabilization in an idealized 2D inviscid semigeostrophic model (MF). In every case we found that the vortex strength, measured by the absolute vorticity, increased steadily with time after an initial adjustment of the vortex to its moist neutral environment. In the presence of an Ekman layer in the three-dimensional model, we find the vortex slowly decays initially, but the potential vorticity generation soon dominates the dissipation and the vortex intensifies. We interpret this initial decay as an adjustment of the vortex to both the Ekman layer and the near-moist neutral environment. If we fix the (nondimensional) Ekman pumping strength at $\delta = 7.14 \times 10^{-2}$, but slightly increase the moist stability parameter to $R_0 = 0.2$, we still find a gradually intensifying vortex. In general, this intensification process proceeds more slowly than the moist baroclinic interaction. Nonetheless, diabatic destabilization appears robust as long as the atmosphere is maintained near moist neutral ($R \to 0$). Experiments with larger R_0 have not been performed, though presumably there is a threshold value R_c above which dissipation becomes dominant and the vortex decays.

Conceptually, the life cycle for midlatitude cyclones that form over land consists of a developmental stage followed by a filling phase in which the cyclone decays by frictional inflow (Bjerknes 1951). Of course, a cyclone's life span can be prolonged by the passage of a nearby mobile trough. In contrast, barring any external influences, the secondary phase of the polar low life cycle is quite different. Polar lows tend to retain their intensity until they move inland (Nordeng 1990). The preceding example illustrates a simple mechanism for maintaining cyclone intensity in the presence of near-neutral static stability for ascent.

As discussed in previous work (MF), a localized vortex will not remain thermally balanced in a surface baroclinic zone without ascending and descending motions. For moist dynamics, surface potential vorticity will be produced in ascent regions. In fact, in the $R \to 0$ limit most of the induced potential vorticity goes directly into absolute vorticity. Thus, depending on the relative magnitudes of friction (δ) and the moist stability parameter (R), spindown may be opposed or reduced by this vorticity-generating mechanism. According to this schematic when polar lows move inland, or move into an area of reduced moist convection, R effectively becomes close to unity and surface friction becomes dominant.

4. Discussion and conclusions

We have investigated the dynamics of polar lows within the context of a three-dimensional geostrophic momentum model that incorporates the condensation process and includes strong baroclinic dynamics. Par-

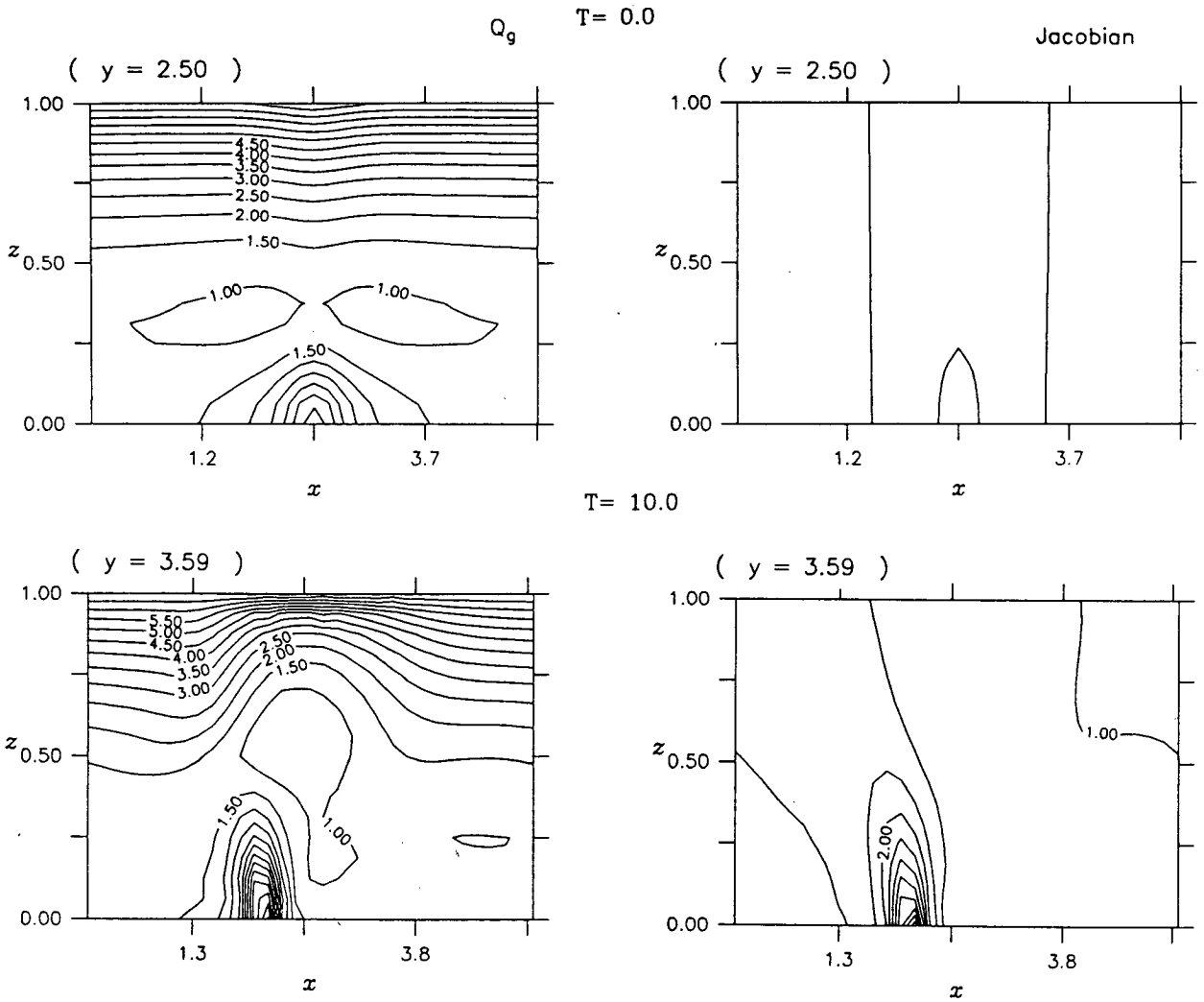

FIG. 4a. Illustration of diabatic destabilization. Snapshots of moist dynamics ($R_0 = 0.1$) for the three-dimensional initial condition given by (3.2) at $T = 0$, and 10.0 advection times (0.0 and 39.6 h, respectively). The left-hand column shows contour plots of the nondimensional total potential vorticity Q_g for $y = 2.50$ and $y = 3.59$. The right column shows contour plots of the Jacobian field for the same y sections. The contour interval for both Q_g and Jacobian is 0.5. Solid lines denote positive values.

ticular emphasis was placed on understanding the influence of upper-level potential vorticity disturbances on the formation process. Remarkably, it appears that even in the absence of cooperative intensification mechanisms, many of the principal features of the mature polar low (i.e., a rapidly forming subsynoptic-scale cyclone possessing hurricane force winds and a relatively warm core) are within reach of this model.

An example of polar low formation in association with interacting upper- and lower-level potential vorticity anomalies in a near-moist neutral environment ($R_0 = 0.1$) resulted in a mature polar cyclone in a period of 25 h. The model storm was characterized by maximum surface winds exceeding 30 m s^{-1}, a horizontal scale of approximately 500 km, a pressure deficit of 26.7 mb, and a relatively warm core near the storm center. A bent-back frontal structure formed in the vicinity of the polar low. At a slightly increased moist stability ($R_0 = 0.2$), an even stronger cyclone forms with a pressure drop of approximately 34 mb, but at a longer time of 35.6 h. In contrast, when this example is run for a dry atmosphere a minimal cyclone is produced with maximum surface winds of 12 m s^{-1} at $T = 25$ h and a weak frontal structure at $T = 40$ h. The scale of the dry storm was comparatively much larger than the moist storms. For upper-level PV anomalies with horizontal scales near the ambient deformation radius, moist processes appear essential for the rapid emergence of the mature subsynoptic storm structure.

Numerical experiments suggest a conceptual model in which polar low development occurs in two stages. The first stage comprises an interaction between upper-level and lower-level potential vorticity anomalies in a nearly moist neutral baroclinic atmosphere. For a

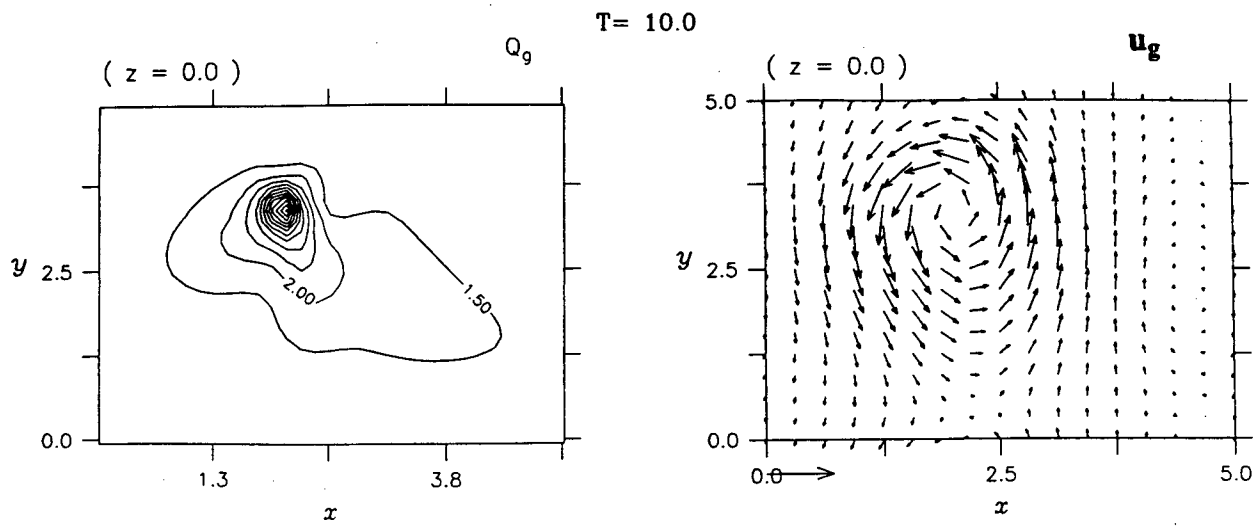

FIG. 4b. Diabatic destabilization continued. As in (a) but shown are horizontal sections of the nondimensional potential vorticity Q_g and the geostrophic wind $\mathbf{u}_g$ on $Z = 0.0$ at $T = 10.0$ (39.6 h). The contour interval for Q_g is 0.5 and solid lines denote positive values. The horizontal vector in the bottom left corner of the $\mathbf{u}_g$ plot corresponds to 30 m s^{-1}. The transformation back to real coordinates is not included in the $\mathbf{u}_g$ plot.

small value of the moist stability parameter, R_0, interpreted here as the deviation from conditional moist neutrality, thermal wind balance requires strong ascending motions ahead of the oncoming trough. The enhanced omega response causes rapid low-level spinup and generation of low- and midlevel potential vorticity anomalies that augment the baroclinic interaction between these systems. A secondary intensification ensues associated primarily with the diabatic production of low-level potential vorticity in ascending regions. For the near-moist neutral case moderate Ekman pumping does not negate this secondary development process. In previous work (MF) we called the moist PV interaction induced self-development (ISD) and the secondary intensification stage diabatic destabilization. Perhaps a more appropriate name for the latter process would be diabatic intensification, though in any event the secondary stage generally proceeds at a slower rate than the primary stage.

In this work we characterize both ISD and diabatic destabilization as finite-amplitude evolutionary processes. The simulated cyclone structures rapidly become nonlinear entities, and they have little to do with slowly growing unstable eigenmodes for either the dry or moist linear instability problems.

Observations indicate that polar lows often maintain their intensity, or slowly intensify until they reach land. Diabatic destabilization represents a simple mechanism for maintaining the intensity of these systems over water provided a suitable portion of the lower atmosphere is maintained nearly moist neutral. In exceptional instances of polar cyclogenesis with negligible upper-level forcing, diabatic destabilization can also describe the gradual intensification of small-scale vortices in regions of sustained neutrality and surface baroclinicity.

The polar cyclogenesis theory described above is related to an earlier conceptual model of polar low development that envisioned development in two discrete stages, an initial phase followed by a secondary phase. Initial development occurred through a dry-adiabatic transient interaction between a mobile upper-level trough and a low-level disturbance, in analogy with the theory advanced for describing midlatitude cyclogenesis (Farrell 1982). The CISK and/or air–sea interaction mechanisms were then invoked for the secondary cyclone intensification phase (Rasmussen 1985; Emanuel and Rotunno 1989; Nordeng 1990). In contrast, our results suggest that both the initial and secondary phases can be viewed as a synthesis of ISD and diabatic destabilization. The dry-adiabatic transient process is obviously contained within this more complete theory, but additional physical mechanisms not included in the present model appear unnecessary for describing the bulk of the formation process. While cooperative intensification processes associated with either CISK or air–sea interaction may be operative in the later phase of development, neither appears essential. Such processes may play the role of a cyclone "afterburner."[3]

We suggest that the relatively warm core observed near the center of polar lows is primarily due to warm-air seclusion, a process in which warm air from the south intrudes into the center of the storm, becomes cut off from its source, and gets surrounded by colder air from the north that is cyclonically wound around the storm. Observations are consistent with this schematic. Model results with moist dynamics show a rapid

[3] We believe the current conceptual model is also applicable to the case of explosive midlatitude cyclogenesis. Model results are transferable by relatively small changes in the three nondimensional parameters given in Table 1.

intrusion of warm air into the storm center, followed by wrapping of colder air around the warm-air patch.

Polar lows often possess a cloud-free "eye" in the center. The inner structure of the more intense polar lows may indeed be similar to the eye of a hurricane with subsiding air in the center and a warm dry core (Businger 1991). In such cases the warm inner core could result from a combination of warm-air seclusion and dry-adiabatic compression. Recall that for a laminar Ekman layer the vertical velocity at the top of the boundary layer does not vanish at the storm center. For a turbulent Ekman layer on the other hand, the vertical velocity at the top of the boundary layer vanishes at the center and increases linearly with radius [Eliassen 1971; Gill 1982, see Eq. (9.5.3)]. Eliassen suggested that the eye structure of a hurricane, with the main ascending currents occurring near the eyewall, may be the result of Ekman layer control. A similar Ekman pumping effect might account for the eye structure of some polar lows. In this work, ascending air in the later developmental phase tends to surround the storm center, and results are consistent with observed cloud patterns taken from satellite images. Present model results, however, do not exhibit subsidence in the center of the storm. Numerical integrations were terminated near the onset of the mature phase, and a hurricane-like inner core may still be within this model's grasp (see comments below).

The formulation of a self-consistent lower boundary condition for the geostrophic momentum approximation has been carried out by Blumen and Wu (1982). Other theoretical work has addressed the nonlinear boundary-layer dynamics of steady (Carrier et al. 1971; Eliassen 1971; Carrier 1971), and time-dependent (Barcilon 1965; Carrier 1971; McWilliams 1971; Eliassen and Lystad 1977) axisymmetric swirling flows. The Ekman condition used in this work was chosen for its simplicity. It would be of interest to compare these formulations in order to assess the sensitivity of the inner-core structure to the parameterized boundary layer. Further observations of polar low interiors and continued research in swirling boundary-layer flows should provide a more complete understanding of the mature inner core of polar lows.

The idealized baroclinic environment used was a uniform meridional temperature gradient plus a tropopause layer. More complex mean flows would have only complicated modeling of the fundamental physical processes, but it is nevertheless important to understand the dynamics of polar lows in more realistic flow settings. Polar lows occur in a variety of flow environments. For example, polar lows often form poleward of the polar jet, giving rise to comma-shaped cloud patterns (Reed 1979). Polar lows are also observed to form in low-level baroclinic zones that are embedded within occluded synoptic-scale cyclones (Bond and Shapiro 1991). Finally, polar lows are sometimes observed to occur in a train or cluster of small-scale cyclones (Reed and Duncan 1987; Rasmussen 1985). Understanding the influences of the flow environment on the formation and the mature structure of polar lows is an important topic for further study.

Recent work of Snyder et al. (1991) has compared the primitive equation (PE) and GM solutions for a specific class of uniform potential vorticity flows. Their study finds systematic difference between the GM and PE models with respect to the horizontal phase tilt of a developing baroclinic wave and the strength of the model anticyclones. However, the strength of the GM cyclone closely matches the strength of the PE cyclone well into the nonlinear life cycle (their day 6.3). Moreover, when the nonlinear Jacobian term (traditionally neglected in GM life-cycle simulations) is retained, the full GM model tracks the PE model a bit more closely than the simpler GM model (see their Fig. 10). Therefore, it seems that the full GM system given by (2.3, 2.4), although not formally valid for high-curvature vorticity flows, may nevertheless capture the essence of the cyclogenesis process. In this work the goal was to develop a conceptual model for polar low formation and the GM system is perhaps the simplest model framework for such a study. While it is possible that the PE model may produce a more pronounced seclusion and an even stronger cyclone in the mature phase, the basic results should nevertheless remain valid. Further scrutiny of the discrepancies between the PE and the GM systems, as well as comparison with other intermediate balanced models (McWilliams and Gent 1980), is indicated for a more accurate understanding of the complete nonlinear life cycle of polar lows.

We have been unable to investigate the fully mature polar low structure. Numerical integrations were terminated when the absolute vorticity exceeded $20f$ since it tended to become infinite shortly thereafter. The primary goal was to illuminate the basic genesis process, but we have shown that much of the mature structure emerges before the onset of the singularity. In fact, were it not for this singularity, model results suggest that a further intensification would occur. A model that allowed continuation of the integration beyond this singularity while also permitting further storm development would be of value. Such a method would perhaps render the GM system integrable for all times and permit study of the fully nonlinear cyclone structure. Recent work has addressed the problem of continuing the GM system beyond the time of singularity formation, T_c, for the case of two-dimensional uniform potential vorticity flows. One method introduces explicit diffusion within the frontal zone to prevent the formation of infinite vorticity in order to provide a more realistic description of dry frontal equilibration (Nakamura and Held 1989; Blumen 1990a,b). Another method entails tracing the development of the frontal discontinuity into the fluid domain for $T \geqslant T_c$ (Cullen 1983; Cullen and Purser 1984; Cho and Koshyk 1989).

A striking feature noted in the moist runs was the rapid scale contraction of the polar low. Scale reduction is ultimately caused by retention of ageostrophic ad-

vections included in the GM approximation, but small R dynamics greatly increases the rate of the contraction process. Physically speaking, dissipative processes should preclude singularity formation and a complete representation of the centrifugal force would ultimately stop the contraction process. The end result would then be a mature subsynoptic cyclone that has equilibrated or is slowly decaying. We surmise that the main parameters that determine the cyclone scale are the initial scale of the upper- and lower-level disturbance; the deviation from moist neutrality R; and the strength of the dissipation. The problem of equilibration and the mature structure remains for future work.

Our approach for studying polar lows is similar in theme to previous work (MF), and we stress the initial-value approach for understanding the cyclogenesis process. Although the physical mechanisms that produce mobile upper-level potential vorticity anomalies are not addressed here, we acknowledge their crucial role in the formation process and choose representative initial conditions that are consistent with observations. We contend that polar lows do not form by spontaneous instabilities, but are driven by potential vorticity disturbances aloft. This theory implies that upper-level tropospheric data are crucial for understanding and predicting the formation of these storm systems.

Taking a more general viewpoint, we hypothesize that the formative mechanisms for polar lows are in fact the same as the formative mechanisms for midlatitude cyclones, with moist processes playing a more central role in the polar low case. We further surmise that the essence of these systems and the great variety of arctic and midlatitude cyclones in the earth's atmosphere can be understood within the context of a simple balanced model framework.

Acknowledgments. This work was supported by NSF ATM-8912432 and by an appointment to the Global Change Distinguished Postdoctoral Fellowships sponsored by the U.S. Department of Energy, Office of Health and Environmental Research, and administered by Oak Ridge Associated Universities. The work was carried out at Harvard University and the Hurricane Research Division—NOAA/AOML in Miami, Florida. Numerical computations were supported by NCAR SCD 35121031. We would like to thank Dr. Allan Robinson for generously providing plotting resources. Dr. Donald Anderson lent advice on numerical methods, Dr. Carlos Lozanos lent advice on the Shapiro filter, and discussions with Dr. Katsuyuki Ooyama, Dr. Lloyd Shapiro, Dr. Chris Snyder, and Dr. Christoph Schär are acknowledged. We thank Dr. Mark Handel for pointing out the Eliassen and Eliassen and Lystad references. We also thank Dr. Alan Thorpe for recommending that we use the omega equation over the two streamfunction equations. Finally, we appreciate the many constructive comments of the reviewers.

APPENDIX

Lower Boundary Condition for the Vertical Velocity

In this Appendix we describe the lower boundary condition for the vertical velocity and summarize its basic properties. While there is no doubt that inviscid models continue to prove useful in our understanding of large-scale atmospheric dynamics, it is certainly not wholly justified to neglect surface friction in life-cycle simulations of cyclones and fronts.

From a dynamics viewpoint, frictional forces induced by the no-slip boundary condition disrupt the primary geostrophic balance and tend to accelerate boundary-layer air toward regions of lower pressure. For an idealized axisymmetric vortex in a resting atmosphere, boundary-layer parcels spiral toward the center and get ejected into the flow above. In the absence of an auxiliary intensification mechanism the induced secondary circulation causes vortex spindown.

From an energetics viewpoint, we expect boundary-layer dissipation to be a substantial part of the mature polar low's energy budget. A recent analytical study incorporating momentum diffusion in 2D frontal zones estimates the viscous dissipation rate to be 250 W m^{-2} for a mature surface front (Blumen 1990b). This is substantially larger than 1–5 W m^{-2}, the average dissipation rate in the planetary boundary layer. It is likely that similar magnitudes are to be found within frontal zones of mature polar lows.

In this work we assume that the primary effects of boundary-layer processes are to maintain moist neutrality in regions of unlimited moisture supply and to redistribute mass between the boundary layer and the flow interior. In theoretical models it is customary to represent the latter process by specifying the vertical velocity at the top of the boundary layer ($Z = 0$). The simplest Ekman formulation equates the vertical velocity on $Z = 0$ to the vertical component of the surface stress curl, and is asymptotically valid in the boundary-layer approximation as the Rossby number tends to zero (Gill 1982). Using the scaling of Table 1 and suppressing explicit time dependence, the nondimensional formula is

$$w(x, y, z = 0) = \delta\left(\frac{\partial}{\partial x}\tau_y^{(s)} - \frac{\partial}{\partial y}\tau_x^{(s)}\right), \quad \text{(A1)}$$

where delta is defined in Table 1, and $\tau_y^{(s)}$ and $\tau_x^{(s)}$ comprise the meridional and zonal components of the surface stress, respectively. Equation (A1) is defined in real coordinates and transformed to geostrophic coordinates below. Also, an explicit formula for the stress is not yet specified. For doubly periodic surface stresses, or vanishing stresses at infinity, the pumping condition (A1) ensures that mass is conserved and merely redistributed between the interior and boundary-layer flow, that is,

$$\int w(x, y, z = 0)dxdy = 0,$$

and integration is taken over the entire horizontal domain.

At Rossby numbers of order unity (A1) is no longer formally justified. For such flow regimes an alternative Ekman formulation that is consistent with the GM approximation has been developed by Blumen and Wu (1982). However, for the purposes of illustrating basic ideas we choose the simpler formulation (A1) in this work. Possible directions for further work concerning the boundary-layer dynamics of mature polar lows are discussed in the conclusion.

Numerical integrations of (2.3, 2.4) are carried out in geostrophic coordinates with (A1) transformed accordingly. The transformation formulas of Hoskins (1975) give, after some simplification,

$$w(X, Y, Z = 0) = \delta J\left(\frac{\partial}{\partial X}\tau_2^{(s)} - \frac{\partial}{\partial Y}\tau_1^{(s)}\right) \quad \text{(A2)}$$

where

$$\tau_2^{(s)} = \tau_y^{(s)}\left(1 + \frac{1}{\sqrt{R_i}}\frac{\partial u_g^{(s)}}{\partial Y}\right) - \tau_x^{(s)}\frac{1}{\sqrt{R_i}}\frac{\partial v_g^{(s)}}{\partial Y},$$

$$\tau_1^{(s)} = \tau_x^{(s)}\left(1 - \frac{1}{\sqrt{R_i}}\frac{\partial v_g^{(s)}}{\partial X}\right) + \tau_y^{(s)}\frac{1}{\sqrt{R_i}}\frac{\partial u_g^{(s)}}{\partial X},$$

and nomenclature is the same as the main text. The lower boundary condition for the omega equation follows from (2.4.b).

In the presence of dissipation the mass-weighted integral of potential vorticity is no longer a flow invariant. A nondimensional tendency equation for the integral of potential vorticity can be obtained directly from (2.3, 2.4) upon transforming to geostrophic coordinates via

$$\frac{\partial}{\partial t}\int Q_g d^3x = \int \frac{\partial}{\partial T}(Q_g J^{-1}) d^3X, \quad \text{(A3)}$$

where integration is taken over the entire flow domain, $d^3x \equiv dxdydz$, and $d^3X \equiv DX\,DY\,DZ$. The rhs of (A3) is further evaluated with the use of (2.3.a) and the evolution equation for the inverse Jacobian (Hoskins and Draghici 1977),

$$\frac{\partial}{\partial T}J^{-1} = -\mathbf{u}_g \cdot \nabla_H J^{-1} - \frac{\partial w^*}{\partial Z}.$$

For doubly periodic flows, or flows that vanish at infinity, the tendency equation simplifies to

$$\frac{\partial}{\partial t}\int Q_g d^3x = \int w^* Q_{g_{\text{eff}}} d^2X = \int w\, Q_{g_{\text{eff}}} d^2x, \quad \text{(A4)}$$

where the rhs of (A4) is evaluated on $Z = 0$, and w^* and $Q_{g_{\text{eff}}}$ are defined in (2.4). We note that (A4) is exact within the stated assumptions of our model, and in particular the heating contribution on $Z = 0.0$ has not been neglected.

In the simple case of dry dynamics with uniform interior PV, the rhs of (A4) vanishes identically since the Ekman layer is mass conserving. In this work we find that Ekman pumping [using (A2) and (2.4.h)] only slightly changes the global integral of potential vorticity for both moist and dry dynamics with nonuniform interior PV. During the course of integrations we monitor changes in the global potential vorticity by evaluating

$$\overline{Q_g} \equiv \frac{1}{(L_X L_Y)}\int Q_g J^{-1} d^3X$$

at each time step using a simple trapezoidal quadrature rule. For the first example of section 2 with $R_0 = 0.1$, numerical values for $\overline{Q_g}$ at $T = 0.0, 3.0, 6.4$ were 2.4014, 2.4086, 2.4106, respectively. Apparently, despite strong Ekman pumping (see Fig. 2b), the ascending and descending contributions to the integral on the rhs of (A4) tend to compensate. We find this to be generally the case.

Further remarks regarding simulations with initial conditions of the form (3.1) are also noted. Without Ekman pumping ($\delta = 0$), but with moderately small moist stability ($R_0 = 0.2$), a well-developed cyclone forms before onset of the vorticity singularity. However, for smaller values of the moist stability ($R_0 = 0.1$), numerical solutions exhibit large vorticities at early times ($\approx$3–4 advection times) and we are unable to integrate beyond this point. In reality, since dissipative processes tend to inhibit singularity formation we believe no generality is lost by adding an Ekman layer on $Z = 0$. For small R ($R_0 = 0.1$), the Ekman layer facilitates integration of (2.3, 2.4) well into the nonlinear phase before singularity formation. Unfortunately, even the quadratic stress parameterization given by (2.4.h) is unable to prevent singularity formation in finite time. Explicit diffusion may be required in the mature stage (e.g., see Blumen 1990a; Nakamura and Held 1989).

REFERENCES

Arakawa, A., 1966: Computational design for long-term numerical integration of the equations of fluid motion: Two-dimensional incompressible flow. Part I. *J. Comput. Physics,* **1,** 119–143.

Barcilon, A. I., 1965: Secondary flow in a viscous vortex. Ph.D. thesis, Harvard University, Cambridge, MA.

Bjerknes, B., 1951: Extratropical Cyclones. *Compendium of Meteorology,* Amer. Meteor. Soc., 599 pp.

Blumen, W., 1979: On short-wave baroclinic instability. *J. Atmos. Sci.,* **36,** 1925–1933.

——, 1990a: A semigeostrophic Eady-wave model incorporating momentum diffusion. Part I: Model and solutions. *J. Atmos. Sci.,* **47,** 2890–2902.

——, 1990b: A semigeostrophic eady-wave model incorporating momentum diffusion. Part II: Kinetic energy and enstrophy dissipation. *J. Atmos. Sci.,* **47,** 2903–2908.

——, and R. Wu, 1982: An analysis of Ekman boundary layer dynamics incorporating the geostrophic momentum approximation. *J. Atmos. Sci.,* **39,** 1774–1782.

Bond, N. A., and M. A. Shapiro, 1991: Polar lows over the Gulf of Alaska in conditions of reverse shear. *Mon. Wea. Rev.,* **119,** 551–572.

Businger, S., 1987: The synoptic climatology of polar-low outbreaks

over the Gulf of Alaska and the Bering Sea. *Tellus,* **39A,** 307–325.
——, 1991: Arctic hurricanes. *Amer. Sci.,* **79,** 18–33.
——, and R. J. Reed, 1989a: Polar lows. *Polar Lows and Arctic Lows,* P. F. Twitchell, E. A. Rasmussen, and K. L. Davidson, Eds., Deepak.
——, and ——, 1989b: Cyclogenesis in cold air masses. *Weather,* **4,** 133–156.
——, and J. Baik, 1991: An arctic hurricane over the Bering Sea. *Mon. Wea. Rev.,* **119,** 2293–2308.
——, and ——, 1991: An arctic hurricane over the Bering Sea. *Mon. Wea. Rev.,* **119,** 2293–2308.
Carrier, G., 1971: Swirling boundary layers. *J. Fluid Mech.,* **49,** 133–144.
——, A. L. Hammond, and O. D. George, 1971: A model of the mature hurricane. *J. Fluid Mech.,* **47,** 145–170.
Charney, J., and A. Eliassen, 1964: On the growth of the hurricane depression. *J. Atmos. Sci.,* **21,** 68–75.
Cho, H. R., and J. N. Koshyk, 1989: Dynamics of frontal discontinuities in the semigeostrophic theory. *J. Atmos. Sci.,* **46,** 2166–2177.
Craig, G., and H. Cho, 1988: Cumulus heating and CISK in the extratropical atmosphere. Part I: Polar lows and comma clouds. *J. Atmos. Sci.,* **45,** 2622–2640.
Cullen, M. J. P., 1983: Solutions to a model of a front forced by deformation. *Quart. J. Roy. Meteor. Soc.,* **109,** 565–573.
——, and R. J. Purser, 1984: An extended Lagrangian theory of semigeostrophic frontogenesis. *J. Atmos. Sci.,* **41,** 1477–1497.
Davis, C., and K. Emanuel, 1990: Potential vorticity diagnostics of cyclogenesis. *Mon. Wea. Rev.,* **119,** 1929–1952.
Duncan, C. N., 1977: A numerical investigation of polar lows. *Quart. J. Roy. Meteor. Soc.,* **103,** 255–267.
——, 1978: Baroclinic instability theory in a reversed shear flow. *Meteor. Mag.,* **107,** 17–23.
Eliassen, A., 1971: On the Ekman layer in a circular vortex. *J. Meteor. Soc. Japan,* **49**(Special issue), 784–789.
——, and E. Kleinschmidt, 1957: Dynamic meteorology. *Handbuch der Physik,* Springer Verlag, 1–154.
——, and M. Lystad, 1977: The Ekman layer of a circular vortex. A numerical and theoretical study. *Geophys. Norweg.,* **31,** 1–16.
Emanuel, K. A., and R. Rotunno, 1989: Polar lows as arctic hurricanes. *Tellus,* **41A,** 1–17.
——, M. Fantini, and A. J. Thorpe, 1987: Baroclinic instability in an environment of small stability to slantwise moist convection. Part I: Two-dimensional models. *J. Atmos. Sci.,* **44,** 1559–1573.
Farrell, B. F., 1982: The initial growth of disturbances in a baroclinic flow. *J. Atmos. Sci.,* **39,** 1663–1686.
——, 1984: Modal and non-modal baroclinic waves. *J. Atmos. Sci.,* **41,** 668–673.
——, 1985: Transient growth of damped baroclinic waves. *J. Atmos. Sci.,* **42,** 2718–2727.
Gall, R. L., 1976: The effects of released latent heat in growing baroclinic waves. *J. Atmos. Sci.,* **33,** 1686–1701.
Gill, A. E., 1982: *Atmosphere–Ocean Dynamics.* Academic Press, 662 pp.
Gronas, S., A. Foss, and M. Lystad, 1987: Numerical simulations of polar lows in the Norwegian Sea. *Tellus,* **39A,** 334–353.
Handel, M. D., 1990: Tropical cyclone intensification from finite amplitude disturbances. Ph.D. thesis, Massachusetts Institute of Technology, Cambridge, MA.
Harley, D. G., 1960: Frontal contour analysis of a "polar low." *Meteor. Mag.,* **89,** 146–147.
Harrold, T. W., and K. A. Browning, 1969: The polar low as a baroclinic disturbance. *Quart. J. Roy. Meteor. Soc.,* **95,** 710–723.
Heckley, W. A., and B. J. Hoskins, 1982: Baroclinic waves and frontogenesis in a non-uniform potential vorticity semi-geostrophic model. *J. Atmos. Sci.,* **39,** 1999–2016.
Hoskins, B. J., 1975: The geostrophic momentum approximation and the semi-geostrophic equations. *J. Atmos. Sci.,* **32,** 233–242.
——, 1976: Baroclinic waves and frontogesesis. Part I: Introduction and Eady waves. *Quart. J. Roy. Meteor. Soc.,* **102,** 103–122.
——, and I. Draghici, 1977: The forcing of ageostrophic motion according to the semi-geostrophic equations and in an isentropic coordinate model. *J. Atmos. Sci.,* **29,** 11–37.
——, M. E. McIntyre, and A. W. Robertson, 1985: On the use and significance of potential vorticity maps. *Quart. J. Roy. Meteor. Soc.,* **111,** 877–946.
Joly, A., and A. J. Thorpe, 1989: Warm and occluded fronts in two-dimensional moist baroclinic instability. *Quart. J. Roy. Meteor. Soc.,* **115,** 513–534.
Mansfield, D. A., 1974: Polar lows: The development of baroclinic disturbances in cold air outbreaks. *Quart. J. Roy. Meteor. Soc.,* **100,** 541–554.
McWilliams, J. C., 1971: The boundary layer dynamics of symmetric vortices. Ph.D. thesis, Harvard University, Cambridge, MA.
——, and P. R. Gent, 1980: Intermediate models of planetary circulations in the atmosphere and ocean. *J. Atmos. Sci.,* **37,** 1657–1678.
Meteorological Office, 1962: *A Course in Elementary Meteorology.* Met. 0.707, Her Majesty's Stationary Office, London, WC1V 6HB, 189 pp.
Montgomery, M. T., 1990: Potential vorticity and diabatic processes in frontal dynamics. Ph.D. thesis, Harvard University, Cambridge, MA.
——, and B. F. Farrell, 1990: Dry surface frontogenesis arising from interior potential vorticity perturbations in a semigeostrophic model. *J. Atmos. Sci.,* **47,** 2837–2852.
——, and ——, 1991: Moist surface frontogenesis associated with interior potential vorticity anomalies in a semigeostrophic model. *J. Atmos. Sci.,* **48,** 343–367.
Mullen, S. L., 1983: Explosive cyclogenesis associated with cyclones in polar air streams. *Mon. Wea. Rev.,* **111,** 1537–1553.
Nakamura, N., and I. M. Held, 1989: Nonlinear equilibration of two-dimensional Eady waves. *J. Atmos. Sci.,* **46,** 3055–3064.
Nordeng, T. E., 1987: The effect of vertical and slantwise convection on the simulation of polar lows. *Tellus,* **39A,** 354–375.
——, 1990: A model-based diagnostic study of the development and maintenance mechanism of two polar lows. *Tellus,* **42A,** 92–108.
——, and E. R. Rasmussen, 1992: A most beautiful polar low. A case study of a polar low development in the Bear Island region. *Tellus,* **44A,** 81–99.
Orlanski, I., 1986: Localized baroclinicity: A source for meso-α cyclones. *J. Atmos. Sci.,* **43,** 2857–2885.
Ooyama, K., 1964: *A dynamical model for the study of tropical cyclone development. Tech. Conf. on Hurricanes and Tropical Meteorology,* Mexico, Amer. Meteor. Soc.
——, 1982: Conceptual evolution of the theory and modeling of the tropical cyclone. *J. Meteor. Soc. Japan,* **60,** 369–380.
Pederson, T. S., 1991: A comparison of the free ride and CISK assumptions. *J. Atmos. Sci.,* **48,** 1813–1821.
——, and E. Rasmussen, 1985: On the cut-off problem in linear CISK models. *Tellus,* **37A,** 394–402.
Rasmussen, E. R., 1979: The polar low as an extratropical CISK disturbance. *Quart. J. Roy. Meteor. Soc.,* **105,** 531–549.
——, 1985: A case study of a polar low development over the Barents Sea. *Tellus,* **37A,** 460–477.
Reed, R. J., 1979: Cyclogenesis in polar air streams. *Mon. Wea. Rev.,* **107,** 38–52.
——, and C. N. Duncan, 1987: Baroclinic instability as a mechanism for the serial development of polar lows. *Tellus,* **39A,** 376–384.
Robinson, A. R., and L. J. Walstad, 1987: The Harvard Open Ocean Model: Calibration and application to dynamical processes, forecasting, and data assimilation studies. *Appl. Num. Math.,* **3,** 89–131.

Sardie, E. R., 1985: A numerical study of the development mechanisms of polar lows. *Tellus,* **37A,** 460–477.

——, and T. T. Warner, 1983: On the mechanism for the development of polar lows. *J. Atmos. Sci.,* **40,** 869–881.

Schär, C., and H. Wernli, 1991: Structure and evolution of an isolated semigeostrophic cyclone. *Quart. J. Roy. Meteor. Soc.*

Shapiro, M. A., L. S. Fedor, and T. Hampel, 1987: Research aircraft measurements of a polar low over the Norwegian Sea. *Tellus,* **39A,** 272–306.

——, E. G. Donall, P. Neiman, and L. S. Fedor, 1990: On the mesoscale structure of extra-tropical marine cyclones. Extended Abstracts, *Fourth Conf. on Mesoscale Processes,* Amer. Meteor. Soc.

Snyder, C., W. Skamarock, and R. Rotunno, 1991: A comparison of primitive equation and semigeostrophic simulations of baroclinic waves. *J. Atmos. Sci.,* **48,** 2179–2194.

Staley, D. O., and R. L. Gall, 1977: On the wavelength of maximum baroclinic instability. *J. Atmos. Sci.,* **34,** 1679–1688.

Thorncroft, C. D., and B. J. Hoskins, 1990: Frontal cyclogenesis. *J. Atmos. Sci.,* **47,** 2317–2336.

Whitaker, J. S., L. W. Uccellini, and K. F. Brill, 1988: A model-based diagnostic study of the rapid development phase of the Presidents' Day cyclone. *Mon. Wea. Rev.,* **116,** 2337–2365.